A model for the simulation of coupled flow-bed form evolution in turbulent flows

Yi-Ju Chou[1] and Oliver B. Fringer[1]

[1] We develop a three-dimensional numerical model to simulate bed form dynamics in a turbulent boundary layer. In the numerical model, hydrodynamics is solved in a moving generalized boundary-fitted curvilinear coordinate system, such that the domain boundary exactly follows complex time-dependent bed form geometry. The resolved turbulent features are computed via large-eddy simulation, while the subgrid scale turbulent motions are modeled with a dynamic mixed model. A second-order accurate arbitrary Lagrangian-Eulerian method is used to guarantee conservation of sediment mass, while the grid moves arbitrarily due to the motion of the bed. Transport of suspended load is modeled using the Eulerian approach with a pickup function as the bottom boundary condition for sediment entrainment at the bed. Transport of bed load and suspended load are combined in a mass balance equation for the bed, which evolves due to the spatiotemporally varying bed stress induced by the turbulent flow field above the bed and gravity (gravity-induced avalanche flow). Motion of the bed in turn affects the flow field in a coupled hydrodynamic moving bed simulation, in which bed features evolve due to resolved details of the turbulent flow. We compare different bed elevation models and demonstrate the capability of the present model through simulation of sand ripple formation and evolution induced by turbulence in an oscillatory flow. A resolution study demonstrates the need for fine grid resolution to resolve a bulk of the near-wall turbulence, which is essential for bed form initiation.

1. Introduction

[2] In the coastal environment and fluvial systems, sediment transport induced by time periodic forcing due to gravity waves or constant forcing due to currents results in different types of bed forms, ranging from small-scale ripples (O (10 cm)) to large-scale (O (10 m)) sand dunes and bars. Understanding bed form dynamics is important because it provides insight into the estimation of the bottom roughness which is of practical importance in coastal and hydraulic engineering. It is also essential in countless problems related to coastal and fluvial geomorphology.

[3] The first models that were employed to study the formation of sand dunes and ripples were based on linear stability theory that required assumptions of weak spatial variability and small-amplitude bed forms [e.g., *Fredsoe*, 1974; *Ridchards*, 1980; *Colombini*, 2004]. In the natural environment, linear stability theory is applicable to the analysis of small-amplitude sand dunes and sand ripples,

namely rolling grain ripples (dunes). Rolling grain ripples are sand ripples over which flow separation does not shed vortices and most of the transport of sediment occurs within the bed in the form of bed load. In the coastal environment where the size of sediment particles is small (O (0.1 mm)), assumption of small-amplitude bed forms is only valid during the initial stages of bed form evolution. This initial period under which rolling grain ripples exist is very short when compared to the time scale of a typical bed form life cycle. In general, ripples continue to grow in size beyond rolling grain ripples and, at a certain amplitude, vortices form in their lee due to flow separation. These vortices provide a strong local vertical velocity field that entrains sediment from the bed into the water column. When the ripples reach an amplitude in which vortices form, they are known as vortex ripples, and sediment transport is dominated by suspended sediment which is ejected into the flow field by the strong vertical velocities and turbulence associated with the vortices. Once vortices form, linear stability analysis no longer applies because of the presence of suspended load, which is primarily responsible for the transition from rolling grain to vortex ripples.

[4] Recently, due to great advances in computational power and computational fluid dynamics (CFD) techni-

[1]Environmental Fluid Mechanics Laboratory, Stanford University, Stanford, California, USA.

ques, great attention has been paid to flow details over vortex ripples. Through numerically solving the discretized Navier-Stokes equations on a rippled bed with oscillatory forcing, simulation results allow detailed observations of the vorticity dynamics [*Blondeaux and Vittori*, 1991; *Scandura et al.*, 2000], turbulence structures [*Barr et al.*, 2004], and sediment transport patterns [*Chang and Scotti*, 2003; *Zedler and Street*, 2006] over synthetic ripples. Although numerical simulations of oscillatory flow over idealized sand ripples reveal realistic flow features and the associated sediment transport phenomena, these studies suffer from the lack of the coupling mechanism between the dynamic bed forms and the flow field. That is, due to the lack of a bed form model to describe the evolution of the bed, these studies are restricted to demonstration of steady or quasi-steady state by assuming a static sand bed. As a result, most of what is known about dynamic bed forms has been realized through laboratory experiments [e.g., *O'Donoghue and Clubb*, 2001; *Faraci and Foti*, 2002; *Testik et al.*, 2005; *Lacy et al.*, 2007]. While laboratory experiments yield a great deal of insight, further understanding of bed form dynamics can be achieved through the use of CFD tools that can simulate the details of the turbulent flow field above a bed and how it leads to the formation of dynamic bed forms which in turn affect the turbulent flow.

[5] Few papers have been published on the numerical simulation of flow problems over dynamic bed forms. *Giri and Shimizu* [2006] present a two-dimensional numerical model that couples the flow field to changes in the bed to simulate sand dune migration in a unidirectional flow. Although they demonstrated predictive capability of their model under some laboratory settings, the simplified two-dimensional model is limited to studying the influence of simplified flow fields on bed form dynamics and cannot be applied to simulate realistic bed forms under complex, turbulent flows. Because formation of bed forms is dominated by turbulence, two-dimensional models cannot directly simulate the formation of bed forms due to a turbulent flow field but instead must model the turbulence to account for the unresolved, three-dimensional flow physics.

[6] A three-dimensional moving bed model is presented by *Ortiz and Smolarkiewicz* [2006] to study large-scale sand dune evolution in severe winds. Combining a numerical atmospheric model with a morphologic model, they successfully obtain qualitatively realistic results of barchan dune evolution in the aeolian system. However, bed form dynamics in water flows is more difficult to simulate than sand dunes in the aeolian environment because morphological dynamics in the aeolian environment results primarily from sand grain saltation and avalanching of granular flows, both of which can be categorized as bed load. In the aquatic environment, on the other hand, morphological processes result from both suspended and bed load transport. Transport of sediment in the atmospheric boundary layer is mainly induced by the shear stress exerted by winds, which in turn influences transport of bed load, while in water, transport of sediment is not only affected by shear stress, but is also closely tied to turbulence and the vortex dynamics of the flow field which contribute to a bulk of the flux of suspended sediment throughout the water column. Therefore, in order to study the detailed flow features and

bed form dynamics in the coastal environment, a three-dimensional Navier-Stokes solver that can resolve fine-scale flow features over time-dependent bottom topography is required.

[7] In this paper, we present a numerical model that solves the Navier-Stokes equations in a moving generalized curvilinear coordinate system. Employing a second-order consistent arbitrary Lagrangian-Eulerian (ALE) scheme, the numerical model solves flow problems on arbitrarily moving meshes, which enables simulation of flows over time-dependent deforming bottom geometry. Moreover, incorporating a suspended load model with the Eulerian approach and a large-eddy simulation model (LES) with a proper sediment boundary condition, the present model is able to simulate sediment pickup and suspension in strongly turbulent flows. Along with a suitable bed elevation model derived from a sediment mass balance, the model enables simulation of unsteady flow and the associated sediment transport over dynamic bed forms, thereby enabling the study of bed form dynamics in complex flows. Unlike previously mentioned studies on numerical simulations of turbulent flow and sediment transport over synthetic fixed ripples, the present numerical model enables study of flow physics and sediment transport over realistic time-dependent ripples. We summarize the mathematical formulation of the present model and we analyze different bed elevation models based on different types of existing empirical sediment transport formulae. Numerical and physical aspects related to the development of the bed elevation model are addressed with simulations of sand ripple formation and evolution induced by turbulence in an oscillatory flow due to waves. The model is validated through comparison to existing numerical and laboratory studies.

2. Mathematical Formulation

2.1. Hydrodynamics

[8] After applying a spatial filter denoted by the overbar, the equations governing the motion of a three-dimensional unsteady fluid with the Boussinesq approximation in strong conservation law form in a generalized curvilinear coordinate system (ξ_1, ξ_2, ξ_3) are given by

$$\frac{\partial \overline{U}_m}{\partial \xi_m} = 0, \tag{1}$$

$$\frac{\partial (J^{-1}\overline{u}_i)}{\partial t} + \frac{\partial (\overline{U}_m \overline{u}_i)}{\partial \xi_m} = -\frac{\partial}{\partial \xi_m}\left(J^{-1}\frac{1}{\rho_0}\frac{\partial \overline{p}}{\partial \xi_m}\delta_{ij}\right) + J^{-1}\frac{\overline{\rho} - \rho_b}{\rho_0}g\delta_{i3}$$
$$+ \frac{\partial}{\partial \xi_m}\left(\nu G^{mn}\frac{\partial \overline{u}_i}{\partial \xi_n} - \mathcal{T}_{i,m}\right), \tag{2}$$

where t is time, u_i represents the Cartesian velocity components, U_m is the contravariant volume flux, δ is the Kronecker delta, p is the pressure, g is the gravitational acceleration, ρ is the density of the sediment-water mixture, ρ_0 is the water density, ρ_b is the background density, ν is the kinematic viscosity, J^{-1} is the inverse of the Jacobian or the volume of the cell, G^{mn} is the mesh skewness tensor, and

$\mathcal{T}_{i,m}$ is the coordinate-transformed subgrid scale (SGS) stress. The quantities U_m, J^{-1}, G^{mn} and $T_{i,m}$ are defined, respectively, by

$$U_m = J^{-1} \frac{\partial \xi_m}{\partial x_j} \overline{u}_j, \tag{3}$$

$$J^{-1} = \det\left(\frac{\partial x_i}{\partial \xi_j}\right), \tag{4}$$

$$G^{mn} = J^{-1} \frac{\partial \xi_m}{\partial x_j} \frac{\partial \xi_n}{\partial x_j}, \tag{5}$$

and

$$\mathcal{T}_{i,m} = J^{-1} \frac{\partial \xi_m}{\partial x_j} \left(\overline{u_i u_j} - \overline{u}_i \overline{u}_j\right), \tag{6}$$

where x_i is the Cartesian coordinate. Here the Einstein summation convention is assumed with $i, j, m, n = 1, 2, 3$ and x_3 is the vertical coordinate. The density stratification of the sediment-water mixture is modeled with

$$\overline{\rho} = \rho_0 \left(1 - \overline{C}\right) + \rho_s \overline{C}, \tag{7}$$

where ρ_s is the sediment density (=2650 kg m^{-3}), and C is the sediment concentration in volume fraction, and in equation (2), the background density, ρ_b, is equal to the water density (ρ_0). In the present study, we employ a dynamic mixed model (DMM) for the SGS motion in the LES framework. The DMM is composed of a dynamic Smagorinsky term and a modified Leonard term. The dynamic Smagorinsky term models the SGS motion as turbulent diffusion with a dynamically determined eddy-viscosity while for the modified Leonard term, through the self-similarity assumption, the other portion of the SGS stress is reconstructed by applying a test filter. In this framework, as is standard practice in LES formulation [e.g., *Zang and Street*, 1995; *Armenio and Sarkar*, 2002; *Cui and Street*, 2004], the impact of the stratification on the unresolved fields is implicit in the method by which the unresolved fields are computed. This occurs because the unresolved fields are either modeled or reconstructed from the resolved fields which are directly affected by density stratification.

2.2. Suspended Sediment

[9] Transport of suspended sediment is modeled with an Eulerian formulation, whereby suspended sediment concentration is transported as a scalar with a settling velocity. In practice, the Eulerian approach can be applied to dilute sediment suspensions with $C \sim O(0.01)$ in volume fraction. However, this assumption may not always be true in coastal flows, particularly in near-bed regions where large concentrations of sediment exist, and under such conditions, two-way coupling effects between sediment and water must be taken into account. The interactions between sediment particles and water can only be modeled with the Lagrangian approach, which tracks the trajectory of each particle and models its own inertia. However, this is not practical to apply to sediment suspension modeling in which a large number of particles are present. An alternate methodology is to employ the two-phase approach, in which sediment parcels are modeled as a second flow phase such that the inertia of sediment parcels and the drag between the sediment phase and water phase is taken into account. However, due to the strong nonlinearity of interactions between groups of sediment particles and the flow, accurate simulation of two-way coupling for sediment-water interaction remains a challenging and unsolved problem, and there is much room for further study, particularly in the context of LES [*Crowe et al.*, 1996]. In the numerical examples that we demonstrate in the present study, since the volumetric sediment concentration in most regions of the domain is less than $O(0.01)$, we employ the Eulerian method, which simulates the sediment dynamics reasonably well in practical engineering problems and has been successfully applied by numerous other authors [e.g., *Gessler et al.*, 1999; *Zedler and Street*, 2001, 2006; *Chou and Fringer*, 2008].

[10] After applying a spatial filter denoted by the overbar, the governing equation for the concentration field (C) of suspended sediment is given by

$$\frac{\partial \overline{C}}{\partial t} + \frac{\partial\left[\overline{C}\left(\overline{U}_m - W_m \delta_{i3}\right)\right]}{\partial \xi_m} = -\frac{\partial \mathcal{F}}{\partial \xi_m}, \tag{8}$$

where W_m is the contravariant settling volume flux and $\mathcal{F}$ is the coordinate-transformed SGS flux, and are defined by

$$W_m = J^{-1} \frac{\partial \xi_m}{\partial x_3} w_s \tag{9}$$

and

$$\mathcal{F}_m = J^{-1} \frac{\partial \xi_m}{\partial x_j} \left(\overline{C u_j} - \overline{C}\,\overline{u}_j\right), \tag{10}$$

where w_s is the settling velocity of the sediment particle. Again, we employ DMM for the SGS sediment flux, which is analogous to DMM for momentum by *Zang et al.* [1993].

[11] A challenging issue for modeling transport of suspended sediment is the bottom boundary condition, which must represent subgrid scale flux of sediment from the bed due to erosion. The pickup function to represent this flux of sediment is given by

$$\frac{P_k}{\sqrt{(s-1)g d_0}} = \begin{cases} \alpha D^{*\beta} T^{*\gamma} & \theta > \theta_c, \\ 0 & \text{otherwise}, \end{cases} \tag{11}$$

where α, β, and γ are constant coefficients to be determined, ρ_s is the sediment density, s is the specific gravity of sediment, g is the gravitational acceleration, d_0 is the sediment diameter, the nondimensional diameter $D^* = d_0 \left[(s-1)g/\nu^2\right]^{1/3}$, $T^* = (\theta - \theta_c)/\theta_c$, the Shields parameter θ is given by

$$\theta = \frac{\tau_b}{(s-1)\rho g d_0}, \tag{12}$$

(a)

(b)
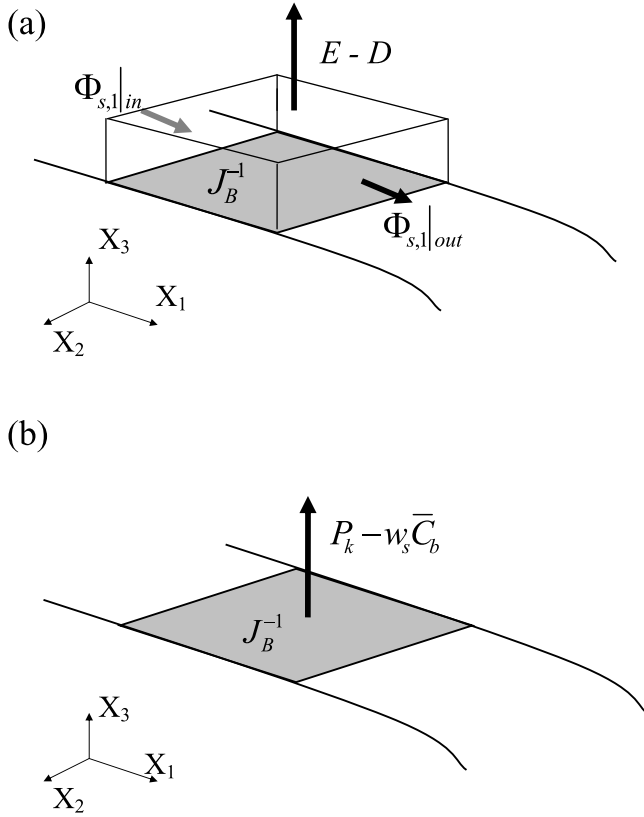
Figure 1. Configurations of the control volume in the BEM with (a) the bed load model and (b) the pickup function.

and θ_c is the critical Shields parameter. The shear stress τ_b at the bottom is calculated with

$$\frac{\tau_b}{\rho} = C_D U_h^2, \tag{13}$$

where $U_h = \sqrt{\overline{u}_1^2 + \overline{u}_2^2}$ is the magnitude of the horizontal velocity, and $\overline{u}_1$, $\overline{u}_2$ are velocity components in the x and y directions, respectively, and C_D is the drag coefficient on the bottom. Based on the log law in the turbulent boundary layer, C_D is determined with

$$C_D = \left[\frac{1}{\kappa} \ln\left(\frac{z_1 + z_0}{z_0} \right) \right]^{-2}, \tag{14}$$

where $\kappa = 0.41$ is the von Karman constant, z_0 is the bottom roughness, and z_1 is the distance between the channel bed and the center of the bottommost cell. On the bed with fixed roughness in the absence of saltating grains, the Nikuradse roughness $z_{0,N} = d_0/12$ can be used as z_0. However, when saltating grains are present, a value that is larger than the Nikuradse roughness should be used. Typically, it varies from $O(0.1d_0)$ to $O(10d_0)$ depending on $T*$ [*Smith and McLean*, 1977; *Grant and Madsen*, 1982]. In the present simulations, Max($T*$) $\approx O(10)$, which gives $z_0 \sim O(d_0)$. Therefore, following *Zedler and Street* [2006], $z_0 = d_0$ is chosen to be the bottom roughness. In the present study, we use the values $\alpha = 0.00033$, $\beta = 0.3$ and $\gamma = 1.5$ in equation (11) as suggested by *van Rijn* [1993] from experimental data. Since the vertical

velocity vanishes at the bottom, the flux described by the pickup function must represent the entire SGS flux from the bed, as described in detail by *Chou and Fringer* [2008].

2.3. Bed Elevation Equation

[12] The bed elevation equation (BEE) mathematically describes the evolution of the bed elevation and provides a link between the fluid motion and the bed form dynamics. In the present study, the bed is defined as the sediment that resides above some immobile layer of sediment and below the fluid. A general form of the mass balance for the sediment within the bed is given in curvilinear coordinates (ξ_m, $m = 1$, 2, and 3) as

$$\frac{\partial J^{-1}\overline{C}}{\partial t} + \frac{\partial \mathcal{F}_{B,m}}{\partial \xi_m} = 0, \tag{15}$$

where $\mathcal{F}_B$ is the contravariant sediment volume flux defined as

$$\mathcal{F}_{B,m} = J^{-1} \frac{\partial \xi_m}{\partial x_j} f_{B,j}, \tag{16}$$

in which $f_{B,j} = \overline{Cu_j}$ is the sediment flux within the bed and is determined by the flow field and local geometry. This transport equation moves sediment around in a very thin layer near the bed in which intensive sediment pickup and deposition result in a very high concentration field. This high concentration field, sometimes referred to as bed load, is the main contribution to bed form dynamics, and the method of modeling this high-concentration sediment-water mixture is the key issue for modeling bed form dynamics.

[13] Assuming δ_B is the thickness of this high-concentration layer, which is also defined as the bed load layer, the depth-integrated mass balance (equation (15)) over δ_B can be written as

$$\frac{\partial J_B^{-1} \delta_B \widetilde{C}}{\partial t} + \frac{\partial Q_{s,n}}{\partial \xi_n}\Big|_{n=1,2} + J_B^{-1}\left(\text{Flux}_{top} - \text{Flux}_{btm} \right) = 0, \tag{17}$$

where J_B^{-1} is a two-dimensional inverse Jacobian (the surface area) of the projected bottom face of the control volume to the horizontal plane, the tilde denotes the average over the thickness δ_B, the subscripts *top* and *btm* denote that the associated quantities are evaluated at the top and bottom surfaces of the bed load layer, respectively, and Q_s is the contravariant sediment volumetric transport rate in the bed plane (the ξ_1, ξ_2 plane). A configuration of this control volume is shown in Figure 1. At the bottom of the bed load layer, the sediment concentration is equal to $(1 - p')$, in which p' is the porosity of the bed material, and the sediment flux at the bottom (Flux$_{btm}$ in equation (17)) can thus be written as

$$\text{Flux}_{btm} = -(1 - p')\frac{\partial h}{\partial t}. \tag{18}$$

Using the notation D and E to represent the deposition and erosion fluxes, respectively, the sediment flux at the top (Flux$_{top}$ in equation (17)) is written as

$$\text{Flux}_{top} = E - D. \tag{19}$$

Substitution of equations (18) and (19) into equation (17) yields

$$\frac{\partial J_B^{-1}\delta_B \widetilde{C}}{\partial t} + (1-p')J_B^{-1}\frac{\partial h}{\partial t} + \frac{\partial Q_{s,n}}{\partial \xi_n}\Big|_{n=1,2} = J_B^{-1}(D - E), \quad (20)$$

where

$$\begin{aligned} Q_{s,n} &= J_B^{-1}\frac{\partial \xi_n}{\partial x_j}\Phi_{s,j} \\ &= J_B^{-1}\frac{\partial \xi_n}{\partial x_j}\int_0^{\delta_B} Cu_j dz, \end{aligned} \quad (21)$$

in which the transport rate $\Phi_{s,j}$ is obtained by integrating the flux over δ_B. Equation (20) describes the bed motion based on sediment mass balance. However, due to difficulties in resolving particle-particle and particle-flow interactions in the near-wall region, several terms in equation (20) need to be modeled empirically. In what follows, we present approaches to model equation (20) and its simplified version employed in the present study.

2.3.1. Bed Load Transport

[14] There have been numerous studies on modeling the transport rate, $\Phi_{s,j}$, in equation (21) using empirical formulae that are functions of the nondimensional shear stress, or the Shields parameter [*Meyer-Peter and Mueller*, 1948; *Fernandez Luque and van Beek*, 1976; *Wilson*, 1987; *Ribberink*, 1998], in which Φ_s takes the form

$$\frac{|\Phi_s|}{d_0\sqrt{(s-1)gd_0}} = C_s(\theta - \theta_c)^b, \quad (22)$$

where C_s and b are coefficients to be empirically determined, and θ_c is the critical shear stress. Using this formula for the magnitude of the flux, the components in each direction, $\Phi_{s,j}$, are obtained with

$$\Phi_{s,j=1,2} = \frac{\overline{u}_{0,j=1,2}}{|\overline{u}_0|}|\Phi_s|, \quad (23)$$

where the subscript 0 implies that the associated quantities are located at the bottom-most cell, and $|\overline{u}_0| = \sqrt{\overline{u}_{0,1}^2 + \overline{u}_{0,2}^2}$. In the present study, we employ the commonly used Meyer-Peter-Muller (MPM) formula for equation (22), in which $C_s = 8$ and $b = 1.5$.

[15] It is important to note that the aforementioned empirical bed load formulae are usually developed under idealized situations such as flat beds and may not be suitable for application to complex cases such as those presented in this paper. Therefore, as we will show, application of only the bed load model to situations in which strong vertical velocity exists, such as flow over sand ripples, leads to over-approximation of the bed load flux because it does not allow entrainment of sediment into suspension.

2.3.2. Erosion and Deposition

[16] When applying equations (22) and (23), the sediment erosion (E) at the bottom boundary is usually modeled using the reference concentration, $\overline{C}_{ref}$, as [*Celik and Rodi*, 1988; *Gessler et al.*, 1999; *Wu et al.*, 2000],

$$E = w_s C_{ref}, \quad (24)$$

in which ($\overline{C}_{ref}$) is derived experimentally in a way that ensures a balance between sediment pickup and deposition in a state of equilibrium. The deposition flux (D) at the bottom is modeled with $w_s\,\overline{C}_b$, where $\overline{C}_b$ is the concentration at the bottom boundary extrapolated from the nearby interior points in the vertical direction. The total flux at the bottom thus becomes $D - E = w_s\,(\overline{C}_b - \overline{C}_{ref})$, and equation (20) becomes

$$\frac{\partial J_B^{-1}\delta_B \widetilde{C}}{\partial t} + (1-p')J_B^{-1}\frac{\partial h}{\partial t} + \frac{\partial Q_{s,n}}{\partial \xi_n}\Big|_{n=1,2} = J_B^{-1}w_s\big(\overline{C}_b - \overline{C}_{ref}\big). \quad (25)$$

Due to the assumption of the equilibrium state under which $\overline{C}_{ref}$ is obtained, this formulation may not properly represent the instantaneous reference concentration in response to strong fluctuations of the flow field and unsteady flows (e.g., waves). Moreover, in equation (25), even if $Q_{s,n}$ and $\overline{C}_{ref}$ are properly calculated, equation (25) is still not closed due to the unknown quantities, δ_B and $\widetilde{C}$.

[17] An alternative to using the reference concentration along with the bed load model is to use the pickup function, which provides a direct link between sediment pickup and the instantaneous shear stress and serves as a Neumann-type boundary condition for the suspended sediment transport model as described in section 2.3.1. One commonly used pickup function was derived by van Rijn in a laboratory setting to determine the magnitude of sediment erosion as a function of particle properties, flow properties, and the shear stress [*van Rijn*, 1993]. There is no further consideration of the transport type after sediment pickup in van Rijn's experiment, and the pickup function accounts for total sediment entrainment including bed load and suspended load. In such a formulation, the layer of the high sediment concentration with thickness δ_B is not explicitly treated but instead is included in the domain of the flow simulation. Thus, equation (20) is written as

$$(1-p')J_B^{-1}\frac{\partial h}{\partial t} = J_B^{-1}\big(w_s\overline{C}_b - P_k\big). \quad (26)$$

Use of the pickup function for sediment erosion assumes that in the near-wall region, intergranular forces are less important when compared to hydrodynamic forces, and that intergranular effects are parameterized in the pickup function. In this framework, there is no need for separate consideration of bed load and suspended load, which is effectively only when sediment transport is dominated by suspension, i.e., there is no substantial layer of high concentration transport in which particulate collision and friction are important. If sediment transport is dominated by a highly concentrated near-wall layer with intensive particulate collision, this layer must be explicitly treated as in equation (25).

[18] Our simulations show that in the absence of the influence of density stratification of the sediment-water mixture, using the pickup function as the bottom boundary condition for suspended sediment transport assumes that sediment is suspended immediately after entrainment from the bed and behaves as a passive scalar. As a consequence, no significant regular geometric variation in the streamwise direction occurs, and unrealistic spanwise geometric varia-

tions are present, as will be shown in a numerical example. We demonstrate that addition of the density stratification term in the fluid momentum equation is necessary for accurate simulation of sand ripple evolution. This effectively models the bed load as a thin layer of high-density fluid near the bed which plays an important role in the formation and evolution of sand ripples.

2.3.3. Gravity Effect

[19] While the shear stresses exerted by the flow on the bed play a dominant role in bed load transport, particularly when the bed is flat, gravitational effects become equally important in the presence of bed forms. We account for gravitational effects on sediment entrainment by modifying the critical Shields parameter (θ_c) in both the bed load formula (equation (22)) and the pickup function (equation (11)). If the Shields parameter for the flat bed is given by $\theta_{c,0}$, then the Shields parameter under the influence of gravity, θ_c, is given by [*Whitehouse and Hardisty*, 1988]

$$\frac{\theta_c}{\theta_{c,0}} = \frac{\sin(\phi_{rp} + \phi)}{\sin(\phi_{rp})}, \qquad (27)$$

where ϕ_{rp} is the bed angle of repose and ϕ is the local bed angle. In the present study, $\theta_{c,0}$ is calculated using an empirical formula which is obtained from the experimental data of *Soulsby* [1997],

$$\theta_{c,0} = \frac{0.3}{1 + 1.2D^*} + 0.055[1 - \exp(-0.02D^*)]. \qquad (28)$$

In a two-dimensional ($x_1 - x_3$ plane) configuration, employing equation (27) is straightforward since ϕ is obtained from the bed slope $\phi = \arctan(dh/dx)$. However, in a fully three-dimensional domain in which geometric variability in the x_2 direction is present, the bed angle is obtained as the bed slope in the direction of the shear stress as

$$\sin(\phi) = \frac{\overline{u}_{1,bed} \sin\phi_1 + \overline{u}_{2,bed} \sin\phi_2}{\sqrt{\overline{u}_{1,bed}^2 + \overline{u}_{2,bed}^2}}, \qquad (29)$$

where the subscript *bed* denotes the velocity component at the bed, and ϕ_1 and ϕ_2 represent the local bed angle in the x_1 and x_2 directions, respectively.

[20] When strongly nonuniform bottom geometry is present such that the local bed slope is larger than the angle of repose, an additional contribution to the transport of bed sediment due to gravity appears. This additional transport rate, denoted by Φ_g, is the gravitational slumping flow which causes the local bed slope to adjust so that it is less than or equal to the angle of repose. Among existing bed load transport models, the empirical formulae are obtained from laboratory or field measurements under mild bed form variability such that the local bed form slope is always less than the angle of repose. As a consequence, there are no empirical formulations available to model Φ_g. One way to model Φ_g is to add a momentum transport equation to the bed load transport as part of the BEE, such that bed load accelerates due to gradients in bed slope that exceed the angle of repose. This leads to equations similar to the

shallow water equations and are analogous to those that are used to model avalanche flow [e.g., *Pitman et al.*, 2003; *Denlinger and Iverson*, 2004; *Mangeney-Castelnau et al.*, 2005].

[21] However, implementation of the shallow water equations to model the bed load leads to several coefficients that are not known due to the lack of laboratory studies on shallow water models for the evolution of bed forms. We avoid the shallow water equations and derive an incremental gravitational flux Φ_g as a slope-dependent quantity such that (as derived in the Appendix A)

$$\Phi_{g,j} = -k\frac{\partial h}{\partial x_j} = -k\frac{\partial \xi_n}{\partial x_j}\frac{\partial h}{\partial \xi_n}|_{n=1,2}, \qquad (30)$$

where the diffusion coefficient, k, is nonzero only when the local bed slope is larger than the angle of repose. The contravariant volume flux ($Q_{g,m}$) of this gravity-induced transport rate ($\Phi_{B,j}$) is then given by

$$Q_{g,m} = kG_B^{mn}\frac{\partial h}{\partial \xi_n}, \qquad (31)$$

where

$$G_B^{mn} = J_B^{-1}\frac{\partial \xi_m}{\partial x_j}\frac{\partial \xi_n}{\partial x_j}|_{m,n,j=1,2}. \qquad (32)$$

Adding the divergence of $Q_{g,m}$ to the BEE with the pickup function (equation (26)) results in

$$(1 - p')J_b^{-1}\frac{\partial h}{\partial t} = \frac{\partial}{\partial \xi_m}\left(kG_b^{mn}\frac{\partial h}{\partial \xi_n}\right)|_{m,n=1,2} + J_b^{-1}\left(w_s\overline{C_b} - P_k\right). \qquad (33)$$

In the present study, we choose the diffusion coefficient,

$$k = \begin{cases} \alpha_k\frac{\phi-\phi_{rp}}{\phi_{rp}}, & \phi > \phi_{rp} \\ 0 & \text{otherwise.} \end{cases} \qquad (34)$$

As shown in Appendix A, the diffusion coefficient k is a function of s, g, δ_B, and the viscosity, μ_S, of the sediment-water mixture in the avalanche layer. Since both δ_B and μ_S vary with sediment properties and the flow shear, it is very difficult to determine a reference value from the existing literature. The effect of k becomes important during mature stages of ripple evolution when ripple slopes become large, i.e., when bed slope > ϕ_{rp}. That is, in a quasi-steady state, time periodic sediment deposition/erosion does not appreciably effect the shape of ripples, and the final shape of ripples is determined by a balance between sediment deposition/erosion and gravity-induced avalanche flow. Therefore, a smaller k will give a steeper bed slope for quasi-steady state ripples. In the present study, we use a value of $\alpha_k = 10^{-4}$ m^2 s^{-1}, which we found to help ensure smooth bed forms without smearing fine-scale features and to give good agreement between the present numerical results and laboratory data. From a numerical perspective, the presence of the diffusion term in equation (33) allows
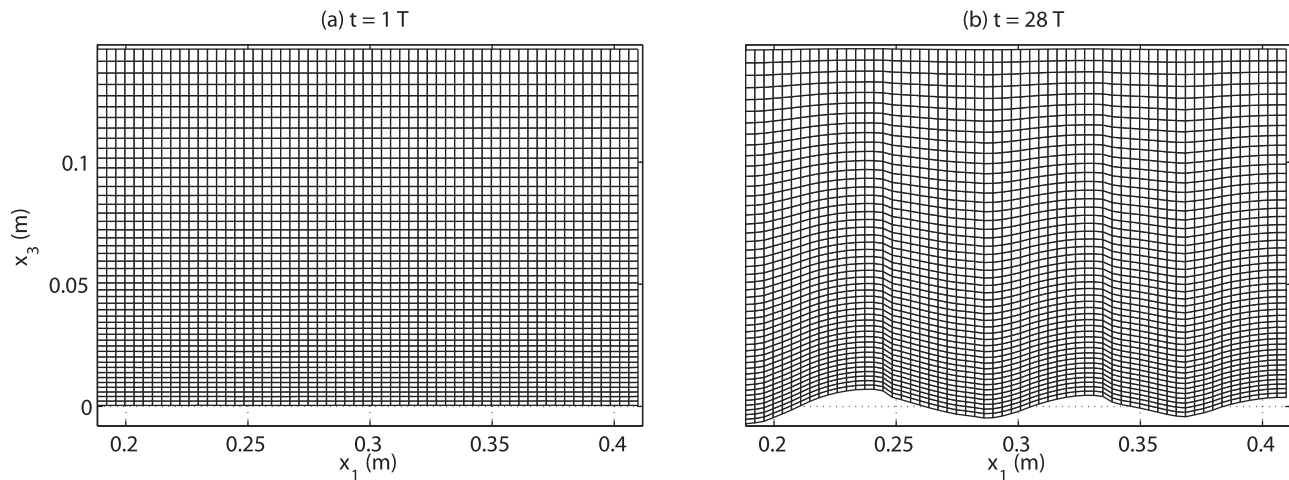
Figure 2. Grid configurations in the x_1, x_3 plane at $x_2 = 0.12$ m and at (a) $t = 1T$ and (b) $t = 28T$ during a simulation of ripple formation under currents. Every other grid line and only a fraction of the domain are shown for clarity.

the BEE to be discretized implicitly in time in a way that ensures smoothness and stability of the resulting bed forms.

3. Numerical Implementation

3.1. Code Description

[22] The aforementioned mathematical formulations are implemented in a CFD code that was originally developed with a generalized fixed curvilinear grid by *Zang et al.* [1994]. In this code, a finite-volume method is used to discretize the governing equations on a nonstaggered grid. All spatial derivatives except the convective terms are discretized with second-order central differences. The convective terms in the momentum equation are discretized using a variation of QUICK (quadratic upstream interpolation for convective kinematics) [*Leonard*, 1979; *Perng and Street*, 1989] and the convective terms in the scalar transport equation are discretized using SHARP (simple high accuracy resolution program) [*Leonard*, 1988]. The second-order Crank-Nicolson scheme is used for the diagonal viscous terms, and the second-order Adams-Bashforth method is used for all other terms. Following *Kim and Moin* [1985], the momentum equation is advanced with a predictor-corrector procedure based on the fractional-step method, in which a divergence-free velocity field is calculated at each time step by correcting the predicted velocity with the pressure gradient. In order to simulate high Reynolds number turbulent flows, a large-eddy simulation (LES) with a dynamic mixed model (DMM) as the subfilter-scale (SFS) turbulence model [*Zang et al.*, 1993] is employed. The code is parallelized using the message passing interface such that it can be run on a parallel computer [*Cui*, 1999]. This code has been successfully applied to simulations of numerous laboratory-scale flows, including turbulent lid-driven cavity flow [*Zang et al.*, 1994], coastal upwelling [*Zang and Street*, 1995; *Cui and Street*, 2004], breaking interfacial waves [*Fringer and Street*, 2005], rotating convective flows [*Cui and Street*, 2001] sediment transport [*Zedler and Street*, 2001, 2006; *Chou and Fringer*, 2008], and free-surface flows [*Hodges and Street*, 1999].

3.2. Mass Conservative Scheme

[23] The grid is allowed to move in response to changes in the bed elevation, and an example of the grid configurations in the x_1, x_3 - plane at different time steps during a simulation is shown in Figure 2. Due to grid motion, special care must be taken when discretizing the transport equation for suspended sediment in order to ensure conservation of suspended sediment mass. To this end, the second-order accurate arbitrary Lagrangian-Eulerian moving grid transport scheme developed by *Chou and Fringer* [2010] is employed. While this scheme ensures conservation of suspended sediment mass under arbitrary grid motion, the total fluid volume within the domain is not necessarily conserved because the equations governing the bed elevation are not required to conserve bed load sediment mass or volume since the bed is an infinite source of sediment. Therefore, in order to ensure compatibility with the incompressible flow solver, which requires that the change in volume of the domain exactly balance the integrated volume flux into or out of the domain, a horizontally uniform vertical velocity is imposed at the rigid lid that exactly balances the change in volume resulting from the evolving bed forms. This vertical velocity is denoted by w_{lid} and is calculated at each step over the time interval $[t^n, t^{n+1}]$ as

$$w_{lid} = \frac{1}{\Delta t} \frac{\mathcal{V}^{n+1} - \mathcal{V}^n}{A_{1,2,top}}, \tag{35}$$

where Δt is the simulation time step, V is the total volume of the computational domain, and $A_{1,2,top}$ is the area of the top surface of the domain.

3.3. Near-Wall Model

[24] In the presence of sediment grains, the channel bed is represented by a rough wall such that the drag law is applied as the bottom boundary condition for the momentum, which is written as

$$(\nu + \nu_T) \frac{\partial u_{1,2}|_{bed}}{\partial x_3} = C_D U_h u_{1,2}|_{bed} \tag{36}$$

$$u_3|_{bed} = 0,$$

where ν_T is the eddy viscosity. In the near-bottom region where the vertically refined pancake-shaped cells are present in order to resolve strong vertical sediment and velocity gradients, following the work of *Chow et al.* [2005], we implement a near-wall model for momentum by augmenting the shear stress with

$$\tau_{1,2,nearwall} = -\int C_c a(z) U_h \overline{u}_{1,2} dx_3, \qquad (37)$$

where C_c is a scaling factor related to the grid aspect ratio, and $a(z)$ (m^{-1}) is a function allowing the smooth decay of forcing as the cutoff height h_c is approached. Since equation (37) serves as a sink in the horizontal momentum equation, in addition to accounting for errors due to the pancake-shaped grid in the near-wall region, it also accounts for the unresolved roughness at the wall [*Nakayama et al.*, 2004]. It also remains as a free parameter to adjust such that the resolved flow field can statistically match the experimental or theoretical results. In the present study, following *Chow et al.* [2005], $a(z)$ is set to cos^2 $(\pi\, x_3/h_c)$ for $x_3 < h_c = 2\Delta x_1$ and zero otherwise, and C_c is obtained from Figure 13 of *Chow et al.* [2005]. A more detailed description of the present near-wall model are given by *Chow et al.* [2005], and successful applications to simulate steady turbulent channel flow with different grid resolutions are presented by *Chou and Fringer* [2008]. In the present study, as shown in Appendix B, comparison of planform-averaged profiles of the streamwise velocity from the present model with the experimental data of *Jensen et al.* [1989] shows good agreement for the case of oscillatory flow over a rough wall.

4. Simulations of the Formation and Evolution of Sand Ripples in Waves

4.1. Simulation Domain and Parameters

[25] In the present study, the simulation is carried out in a three-dimensional domain of size $L_1 \times L_2 \times L_3 = 0.6$ m $\times$ 0.24 m $\times$ 0.15 m. The grid resolution is $N_1 \times N_2 \times N_3 = 320 \times 128 \times 96$ with grid stretching in the x_3−direction, resulting in a minimum grid spacing in the vertical direction of $\Delta x_{3,min} = 0.0011$ m at the bed. The periodic boundary condition is applied to all horizontal boundaries. Since horizontal periodicity may affect the resulting ripple size, the streamwise dimension of the computational domain is chosen such that it contains at least 3 sand ripples throughout the simulation based on laboratory observations [*Lacy et al.*, 2007]. Therefore, the resulting ripple wavelength is not affected by the periodic boundary condition.

[26] The oscillatory flow is simulated by forcing a time periodic pressure gradient with period $T = 8$ s, yielding a maximum freestream velocity of $U \approx 0.4$ m s^{-1}. The oscillatory flow parameters are chosen to match those in the giant flume experiment conducted by *Lacy et al.* [2007] (run 11). The simulations are first run for three wave periods, after which time the sediment models are switched on. In what follows, all times are relative to this point and are normalized by the wave period T.

[27] The particle diameter of $d_0 = 0.27$ mm is used as the size of the sediment particles, which is the same as the mean grain diameter of the well-sorted sediment used by *Lacy et al.* [2007]. Given this grain size and the flow conditions,

particle-particle collision is not a dominant momentum exchange in the near-wall region. The computational time step is $\Delta t = 0.002$ s at early stages when there are no significant ripple marks and $\Delta t = 0.001$ s when ripples are present. At later stages when ripples with large amplitudes develop, $\Delta t = 0.0005$ s. These time steps are chosen to maintain a stable flow simulation, i.e., Max(CFL) $\approx 0.8 < 1$, and are small enough to resolve ripple evolution at every stage because the time scale associated with ripple evolution is larger than $O(0.001$ s$)$. The computations are carried out on the LinuxNetwork Xeon EM64T cluster at the Army Research Laboratory Major Shared Resource Center using 40 processors $(P_x \times P_y \times P_z = 10 \times 4 \times 1)$. The total simulation wall clock time is roughly 3.3 h for one wave period (8 s) at early stages and 13 h at later stages, and simulations require 6.6 Gb of memory. The laboratory experiment was run for 40 min, and ripples reach a statistically-steady state at about 10 min. Since we focus on transient flow and ripple dynamics, and a simulation for the entire 40 min duration requires considerable computational time, we only run the simulation for 11 min of physical time from an initially flat bed, and this requires 47 days of wall clock time, or 45120 CPU h.

### 4.2. Simulation of Sand Ripple Evolution

[28] Figure 3 shows the bed elevation at different stages of sand ripple evolution in the presence of oscillatory flow. The sand bed is initially flat and, other than a few small perturbations, remains relatively unchanged during the first three wave periods. During this initial stage, due to the low near-bed concentration of suspended sediment, the random distribution of sediment deposition and erosion does not result in any permanent bed forms (see Figure 3a). Spatially regular, but not significant, three-dimensional bed forms only appear roughly at $t = 6T$. As shown in Figure 3b, these ripples have a wavelength of approximately 6.5 cm and amplitude of approximately 0.3 cm and exhibit sinuous crestlines. Due to their small amplitude, the crestlines move slightly in response to the oscillatory flow field, as shown in Figure 4. This is consistent with the idea that permanent local sediment erosion and deposition are enhanced by the periodic nature of the flow and the local bed geometry. At this stage, sediment motion is confined to a very thin layer close to the bed (see Figure 5). Movement of this near-bed sediment due to the near-bed turbulent events dominates the bed form initiation. The oscillatory sediment motion results in a continuous growth of ripple crests, leading to more significant ripple patterns with increasing amplitude, as shown in Figure 3c. During the period $0 \le t \le 18T$ (Figures 3a–3d), the amplitude of the bed forms is not large enough to shed strong vortices in their lee. Therefore, although some sediment is suspended intermittently in the lee of small sand ripples during flow acceleration, this suspension is not strong enough to alter the shape of the ripples, as shown in Figures 5 and 6. As a result, ripples are dominated by the three-dimensional structures (e.g., bifurcations and sinuous crestlines) resulting from initial ripple marks.

[29] After $t \approx 18T$, the initial three-dimensional ripples continue to grow and the lee side of the ripples continues to increase in steepness (Figure 3e) until vortices are shed during flow acceleration. Until this stage, bed form evolution can be described by the following four mechanisms, as
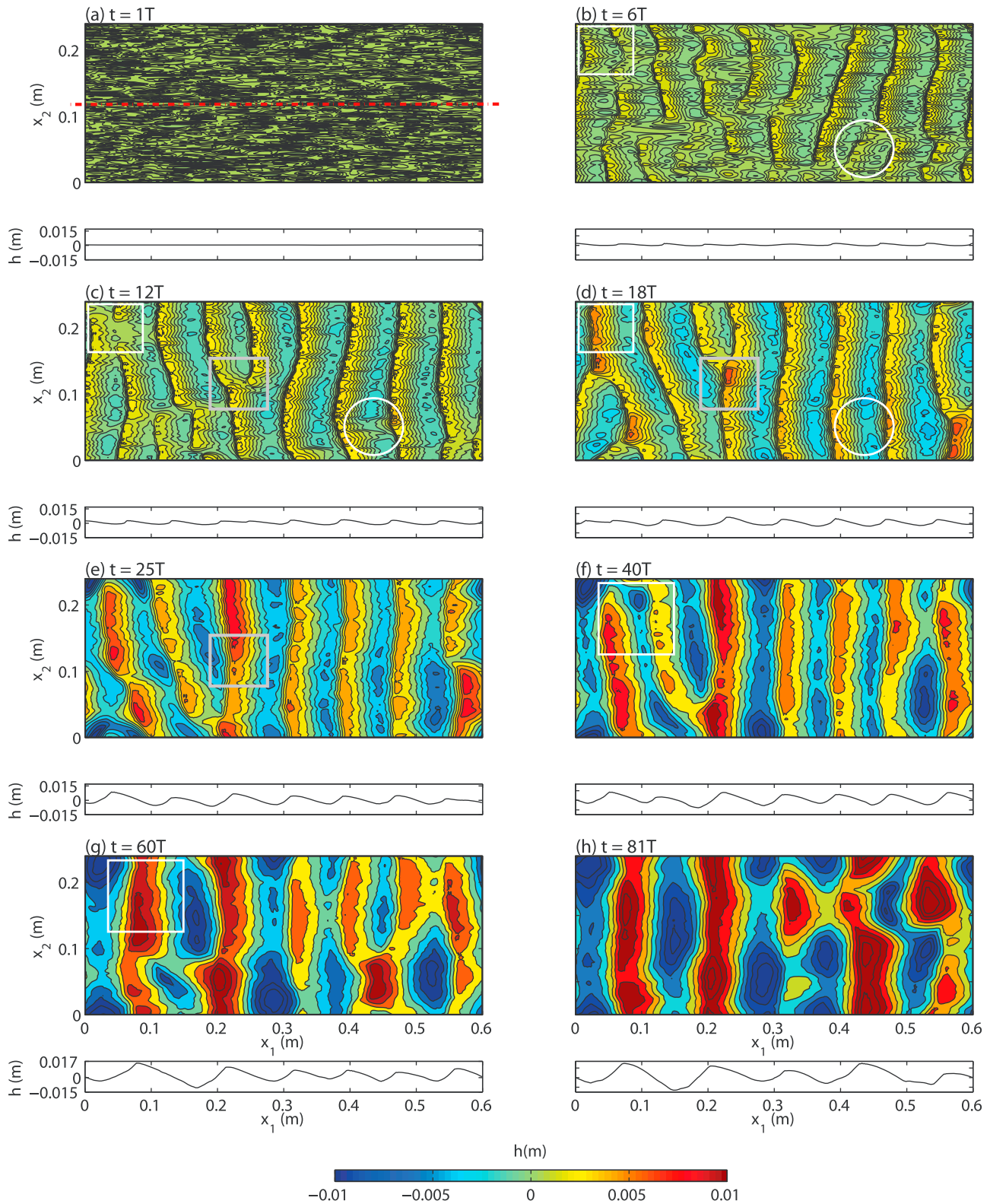
Figure 3. Bed elevation contours and bed form profiles along the channel centerline marked with the red dash-dotted line in an oscillatory flow at (a) $t = 1T$, (b) $t = 6T$, (c) $t = 12T$, (d) $t = 18T$, (e) $t = 25T$, (f) $t = 40T$, (g) $t = 60T$, and (h) $t = 81T$, showing merging of ripples (white squares), vanishing of a small crest-line (white circles), and vanishing of an initial bifurcation (gray squares).
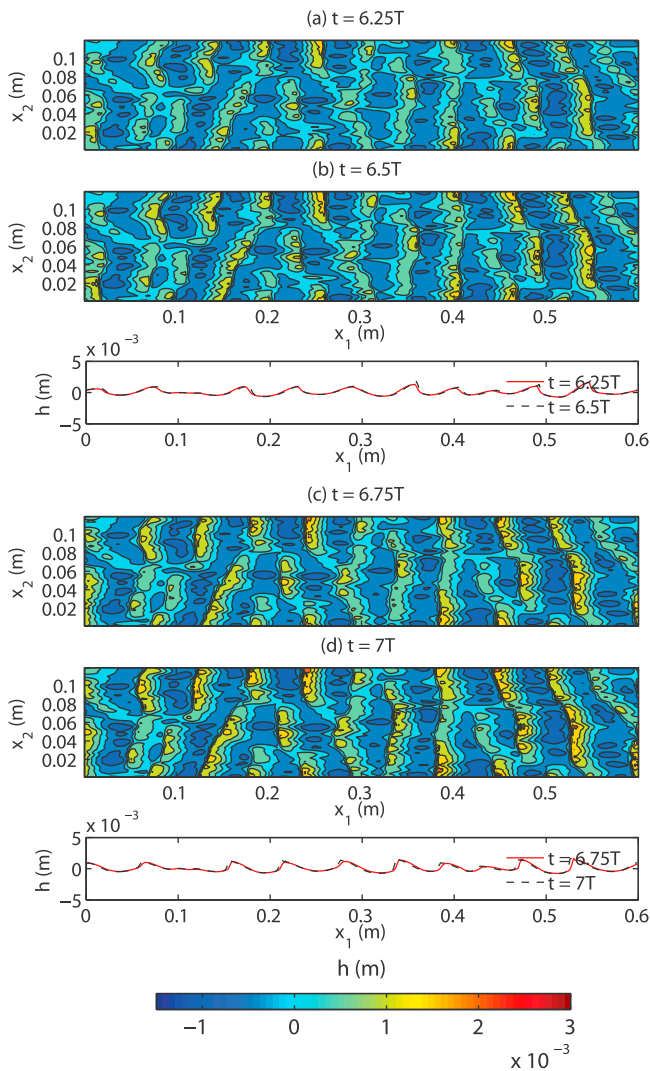
Figure 4. Contours of the bed elevation, showing the response of initial ripple marks to an oscillatory current at (a) $t = 6.25T$, (b) $t = 6.50T$, (c) $t = 6.75T$, and (d) $t = 7.00T$ modeled with the Type 2 BEM (MPM formula).

depicted in Figures 3b–3g: (1) vertical growth due to periodic deposition and erosion; (2) merging of small crests; (3) vanishing of small crests behind large crests due to erosion; and (4) and vanishing of initial bifurcations. The first mechanism is demonstrated in Figure 4, and examples of the other mechanisms are demonstrated in Figure 3. As shown in Figure 3e, at $t = 25T$, other than in the region from $x = 0.1$ to 0.2 m where the sinuous crestlines remain, the bed form exhibits a strongly two-dimensional structure. The transition from three-dimensional to two-dimensional bed forms results from the second, third and fourth mechanisms.

[30] When vortices are shed in the lee of the sand ripples, considerable sediment is suspended by the strong vertical flow, and this sediment is transported further into the water column by the vortices, as shown in Figure 7. Unlike the intermittent suspension characteristic of the initial phase of ripple development as in Figures 5 and 6, the strong vortices induce cross-ripple suspension, which persists throughout each wave cycle. The sand ripples at this stage become

vortex ripples, and their characteristic wavelength scales with the particle excursion. As the ripples continue to grow in amplitude, the size of the associated vortices becomes so large that adjacent ripples are eroded, as shown in Figures 3f and 3g. This mechanism leads to an important transition stage from small three-dimensional ripples to two-dimensional ripples with a larger wavelength. In contrast to the early stages of ripple development in which the evolution is dominated by periodic erosion and deposition of sediment onto the bed, sediment suspension by the vortices during this transitional stage dominates the growth of sand ripples. In addition to suspension due to strong vortices, merging of small ripples to form larger ripples also accounts for a bulk of the dynamics during this transitional stage. After this transitional stage, large and more stable ripples are formed, as depicted in Figure 3f.

4.3. Comparison With the Laboratory Experiment

[31] Under the action of waves, bed forms are initiated due to random turbulence-induced near-bed transport. Ripples first appear as sinuous crestlines which soon evolve into regular ripple patterns. As the bed forms continue to grow in amplitude, they shed vortices and initial small three-dimensional ripples evolve into larger three-dimensional ripples. Our modeling results reveal all of these processes, including transition from small perturbations to small three-dimensional ripples, and from small three-dimensional ripples to larger two-dimensional ripples. The simulation reveals the pattern coarsening process of sand ripple evolution under waves which has been consistently observed in numerous laboratory experiments [*O'Donoghue and Clubb*, 2001; *Faraci and Foti*, 2002; *Andersen et al.*, 2002], but never before in three-dimensional numerical simulations.

[32] Compared with the laboratory observations in run 11 of *Lacy et al.* [2007], which has the same parameters as we use in the present simulation, the mechanisms of transition from two-dimensional to three-dimensional ripple structures and from the small- to the large-amplitude ripples are similar. Figure 8 presents the sonar images from the laboratory experiment and bed elevation contours from the present simulation at certain time steps, which shows that the present simulation captures similar patterns as observed in the laboratory. There are two transitional stages of the wavelength observed in both the numerical simulation and the laboratory experiment. The first stage is the formation of ripple marks (Figure 8a), which is immediately followed by ripple coarsening (Figure 8b). The second stage occurs when small ripples merge to form larger ripples, which forms thicker crest lines (Figures 8c and 8d). These two processes can be observed in both the laboratory and the numerical results, which demonstrates the model ability of obtaining real features of ripple evolution.

[33] Time histories of the averaged wavelength obtained with a two-dimensional fast Fourier transform (FFT) within $\pm 15°$ of the orientation of the wave ripples for both laboratory and model results are shown in Figure 9, along with the wavelength data counted visually. The visually-counted wavelength is obtained by dividing the total distance along a line in the streamwise direction with the counted crest number. The counting process is repeated at three different locations in the spanwise direction to calculate the mean,
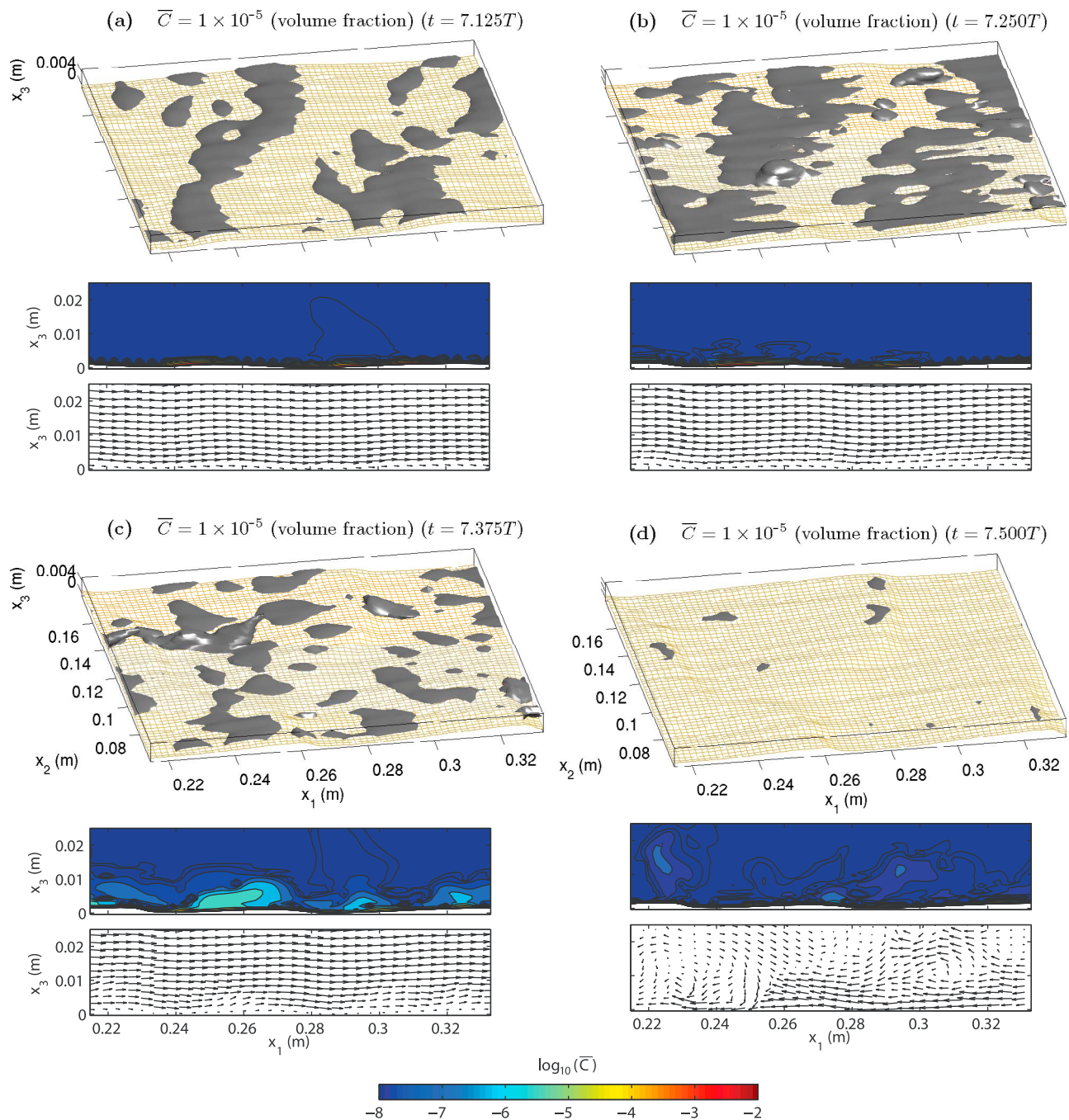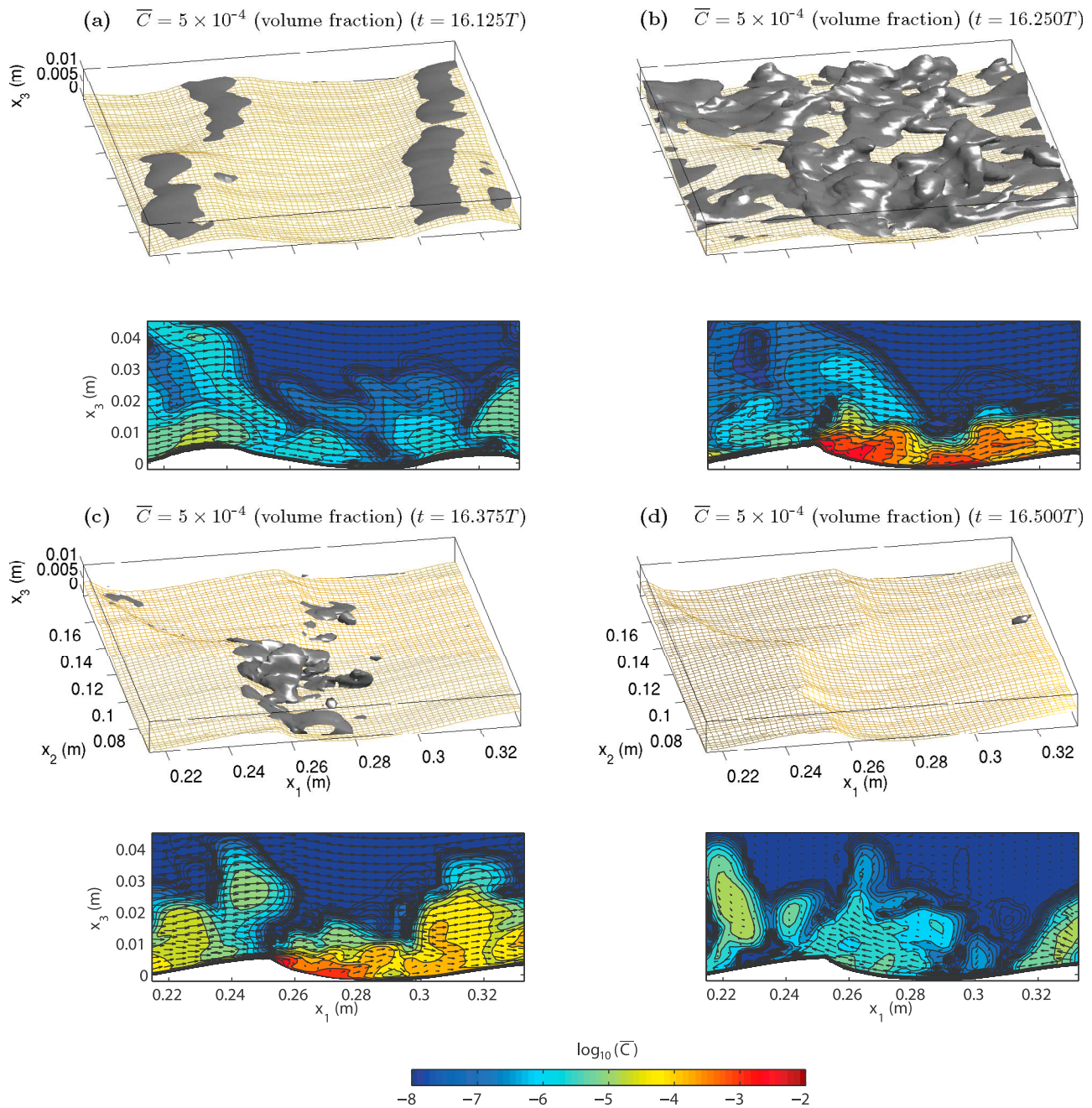
Figure 5. Concentration isosurface of $\overline{C} = 10^{-5}$ (volume fraction) along with suspended sediment concentration contours and velocity vectors in a vertical plane for an oscillatory current at $y = 0.12$ m at (a) $t = 6.125T$, (b) $t = 6.250T$, (c) $t = 6.375T$, and (d) $t = 6.500T$, showing that during the beginning stage of ripple formation, high sediment concentration is confined to a very thin layer close to the bed.

maximum, and minimum values. The orientation of the wave ripples is defined as the direction parallel to the crest over the range −90 to 90°, where 0° is aligned in the direction perpendicular to the wave direction. In the laboratory setting, the FFT is applied with 1-volt amplitude as the threshold between the measured data and noise [*Lacy et al.*, 2007]. In Figure 9, during the initial stage when ripple marks begin to form (0–2 min), ripple wavelengths

calculated from the model results (≈0.065 m) are smaller than the wavelengths calculated by either the FFT or by visually counting the laboratory results. This is due to the fact that at the initial stage, near-wall turbulence is not strong enough to induce significant sediment suspension, such that formation of initial bed forms mainly results from shear-driven bed load, which is not explicitly treated in the present modeling framework. The present model simulates

Figure 6. Concentration isosurfaces of $\overline{C} = 10^{-5}$ (volume fraction) along with suspended sediment concentration contours and velocity vectors in a vertical plane for an oscillatory current at $y = 0.12$ m at (a) $t = 16.125T$, (b) $t = 16.250T$, (c) $t = 16.375T$, and (d) $t = 6.500T$, demonstrating how sediment suspension is intermittent in the presence of small ripples.

sediment suspension and saltation but neglects sediment transport within a layer in which collisions and friction are important and transport is mainly driven by the flow shear.

Therefore, one would expect that in reality, transport of the bed sediment results in faster ripple formation at the initial stage. This initial ripple pattern, which is called rolling grain

Figure 7. Concentration isosurfaces of $\overline{C} = 10^{-5}$ (volume fraction) along with suspended sediment concentration contours and velocity vectors in a vertical plane for an oscillatory current at $x_2 = 0.12$ m at (a) $t = 40.125T$, (b) $t = 40.250T$, (c) $t = 40.375T$, and (d) $t = 40.500T$, showing that compared with Figure 6, sediment suspension is much stronger and persistent due to the presence of vortices in the lee of the vortex ripples.
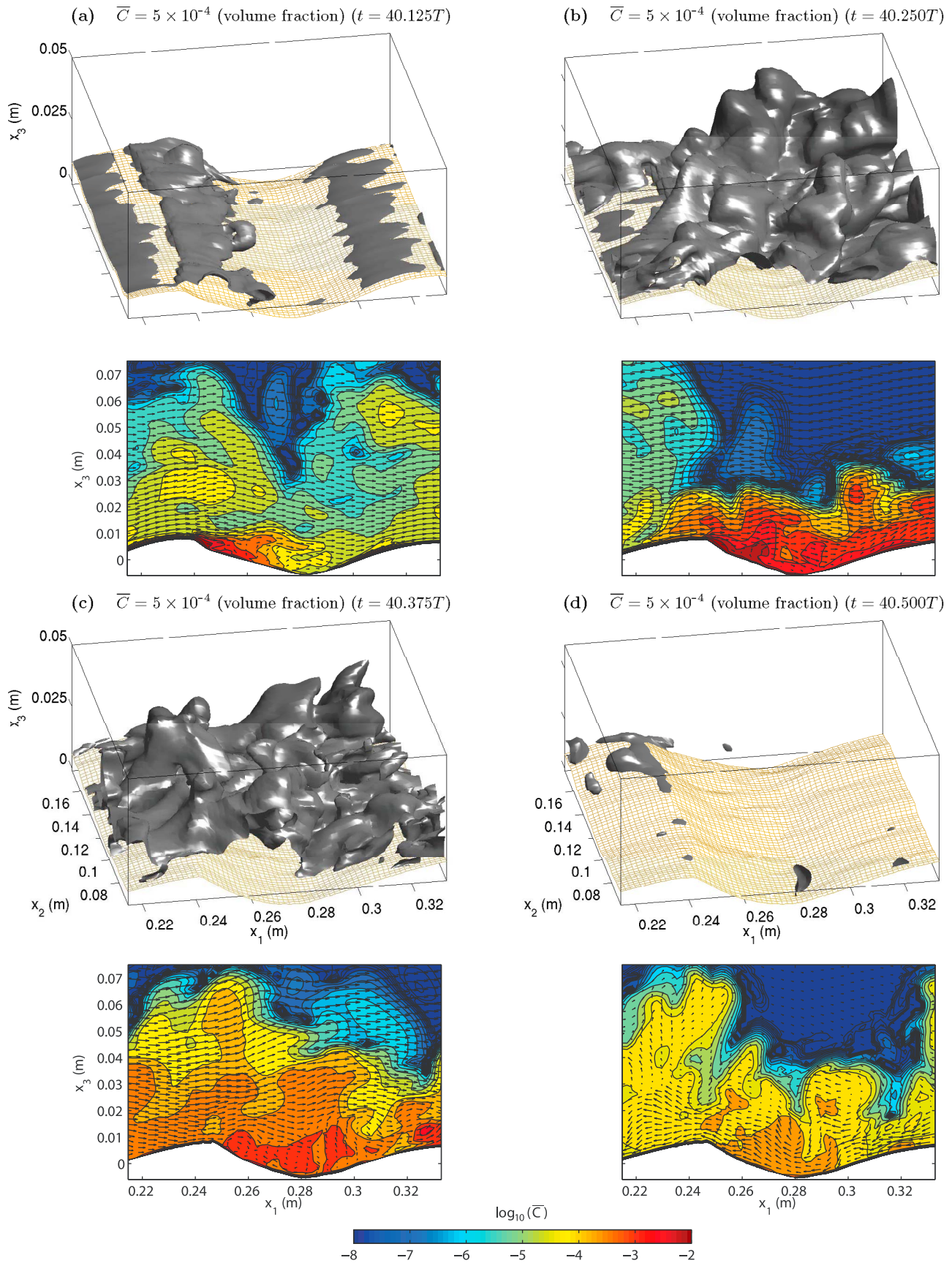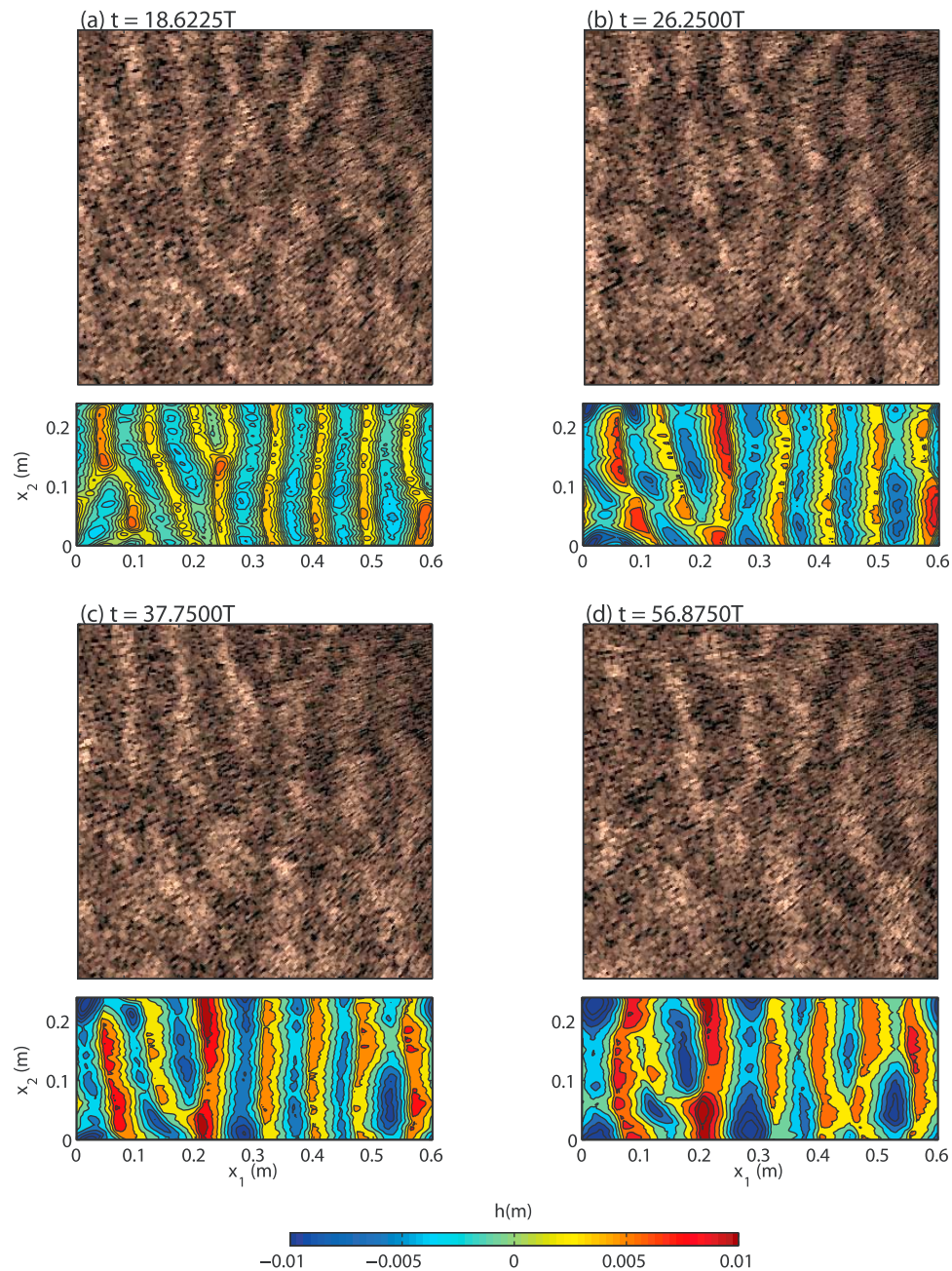
(a) $\overline{C} = 5 \times 10^{-4}$ (volume fraction) $(t = 40.125T)$

(b) $\overline{C} = 5 \times 10^{-4}$ (volume fraction) $(t = 40.250T)$

(c) $\overline{C} = 5 \times 10^{-4}$ (volume fraction) $(t = 40.375T)$

(d) $\overline{C} = 5 \times 10^{-4}$ (volume fraction) $(t = 40.500T)$

$\log_{10}(\overline{C})$

Figure 7

Figure 8. Model results (bed elevation contours) along with sonar images from the laboratory experiment of *Lacy et al.* [2007], comparing the evolution of ripples under waves.

ripples, is not captured by the present model. This is demonstrated in section 5, where we employ the MPM formula to show that it results in faster and larger bed forms at the initial stage. Since most bed load transport models are derived from the condition in which flow is so strong that bed forms are washed out and the bed remains flat, applying the bed load transport model leads to an unstable bed (see section 5). The effect of bed load transport soon becomes minor when bed forms are present because near-wall turbulence is strong enough to entrain significant amounts of sediment, such that suspension dominates sediment transport, which occurs for $t > 2$ min in the present simulation.

After $t \approx 2$ min, the modeled wavelength matches experimental data well and is close to the maximum value of the visually-counted wavelength, which is typically the value between the visually-counted mean wavelength and the FFT wavelength. During the final stage approaching the end of the simulation ($t > 10$ min), the growth rate of the wavelength becomes much slower and evolution of the ripples becomes quasi-steady, which is consistent with the laboratory observations.

[34] Although the ripple height is not monitored during ripple evolution in the laboratory experiment, it is reported by averaging 5 measurements at the end of the experiment.
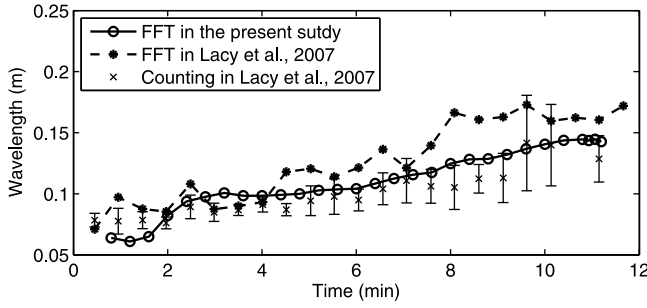
Figure 9. Time histories of the FFT-derived wavelength of sand ripples in the laboratory experiment of *Lacy et al.* [2007] (dashed line) and in the present simulation (solid line), along with the wavelength counted visually in the work of *Lacy et al.* [2007].

In the present simulation, the final statistically-steady wave height is roughly 3 cm, and is close to the final wave height of 3.4 cm measured at the end of the laboratory experiment.

5. Bed Elevation Model Comparison

[35] To demonstrate the effects of the different bed elevation model (BEM) implementations, we simulate the evolution of sand ripples under the influence of waves using three different models. Equation (26) is used in both the first (base) and third models (Types 1 and 3) while there is no stratification effect due to sediment in the third model (Type 3). In the second model (Type 2), the MPM formula is employed in the BEE, and is given by

$$(1 - p')J_B^{-1}\frac{\partial h}{\partial t} + \frac{\partial Q_{s,n}}{\partial \xi_n}|_{n=1,2} = J_B^{-1}w_s(\overline{C}_b - \overline{C}_{ref}), \quad (38)$$

which is the original BEE (equation (25)) but neglects the time variation of $\delta_B \overline{C}$. Although this is not true in the case of unsteady flow, it is neglected to allow for comparison of different BEMs and allows us to demonstrate the effectiveness of different approaches in the literature [e.g., *Gessler et al.*, 1999]. The BEMs employed in all three cases are summarized in Table 1. Simulations are run for 6T, and a smaller domain of size 0.6 m × 0.12 m × 0.1 m but with the same resolution as in section 4 is used for the BEM comparison as well as the resolution study in section 6.

[36] Figure 10 illustrates different bed forms at $t = 6T$ resulting from different BEMs under the influence of waves. As shown in Figure 10b, using the Type 2 BEM results in ripples with a larger wavelength than those produced by the Type 1 model. This is due to the overestimate of bed load transport using the MPM formula (equation (22)) along with equation (38), which, as shown in Figure 11, leads to faster movement of the ripples and a much shorter evolutionary time scale when compared to laboratory observations [*Lacy et al.*, 2007]. As a result, the Type 2 BEM is unable to produce

Table 1. Summary of Components Used in Different BEMs

| BEM	Mass Balance	Density Stratification
Type 1	equation (33)	yes
Type 2	equation (38)	yes
Type 3	equation (33)	no
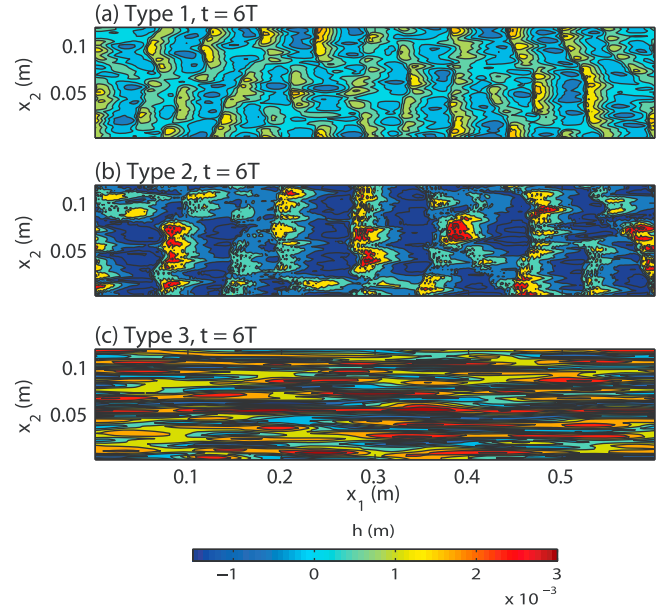
Figure 10. Contours of the bed elevation in an oscillatory flow at $t = 6T$ using the (a) Type 1, (b) Type 2, and (c) Type 3 BEMs.

the stationary ripples that are produced by the Type 1 model. Furthermore, the fast movement and growth result in a steep slope in the lee of the ripple crests during flow acceleration, and during flow reversal the local velocity becomes strong in the stoss of the crests (the original lee side before reversal) due to their steep slope. The steep slopes and fast moving ripples also lead to numerically induced oscillations in the bed evolution. As a result, a restrictive constraint on the simulation time step is required to maintain computational stability. For example, at $t = 9T$, in the Type 1 BEM, a time step of $\Delta t = 0.001$ s results in $CFL_{Max} = 0.62$ while in the Type 2 BEM, a time step of $\Delta t = 0.0005$ s results in $CFL_{Max} = 0.72$. In the Type 3 BEM, due to the absence of the effects of stratification, the sediment has no effect on the flow once it is ejected from the bed. As shown in Figure 10c, the result is to suppress the formation of ripples while enhancing small-amplitude and short-wavelength streamwise variability in the bed forms. Due to the lack of the stratification effect of the near-bed suspended sediment, the near-bed turbulence is enhanced and the bed simply responds to the shear induced by the streamwise coherent structures in the turbulent flow which is unimpeded by stratification. Figure 12 depicts the planform-averaged concentration from the Type 1 and Type 3 models at $t = 4.25T$, which is defined by

$$\widetilde{\overline{C}} = \frac{1}{LW}\int_0^W \int_0^L \overline{C}(x_1, x_2, x_3, t)dx_1 dx_2. \quad (39)$$

The results show that without density stratification, the Type 3 model results in more sediment entrainment and turbulent mixing in the water column. Because the turbulence is so strong, there is no near-bed region to effectively act as the bed load model and lead to the formation of ripples.

[37] By comparing the three approaches that are widely used in the study of sediment transport, these results show
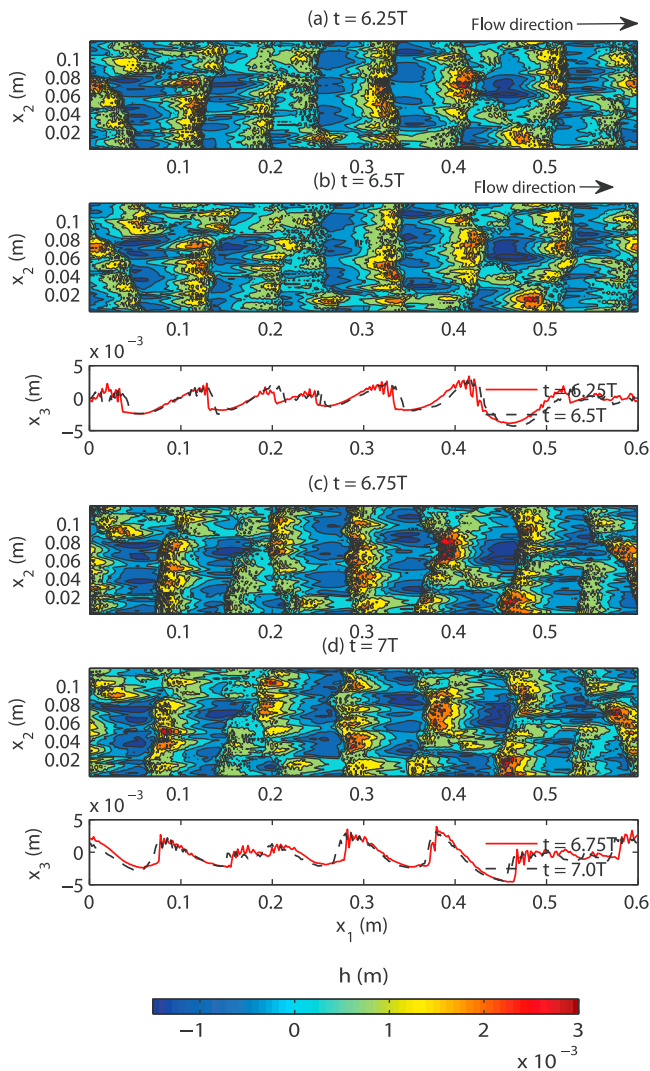
Figure 11. Contours of the bed elevation in an oscillatory flow at (a) $t = 6.25T$, (b) $t = 6.50T$, (c) $t = 6.75T$, and (d) $t = 7.00T$ modeled with the Type 2 BEM (MPM formula), showing how ripple motion is too fast when compared to that using the Type 1 BEM in Figure 4. Line plots depict bed form profiles along the channel centerline and indicate that the fast ripple motion induces numerical oscillations in the bed forms.

that the most effective means of simulating bed load transport is to model it as a highly stratified region near the bed (using the Type 1 BEM) rather than explicitly trying to compute it with only a bed load model (Type 2 BEM). The disadvantage to this approach is that it implies that the bed load transport must effectively be simulated rather than modeled, in that the simulation code must resolve the near-bed turbulent structures that are tightly coupled to the dynamics of the stratified layer near the bed. The importance of resolution is discussed in section 6.

6. Resolution Study

[38] Because initiation of the bed forms results from near-bed turbulence that must be resolved rather than modeled, in
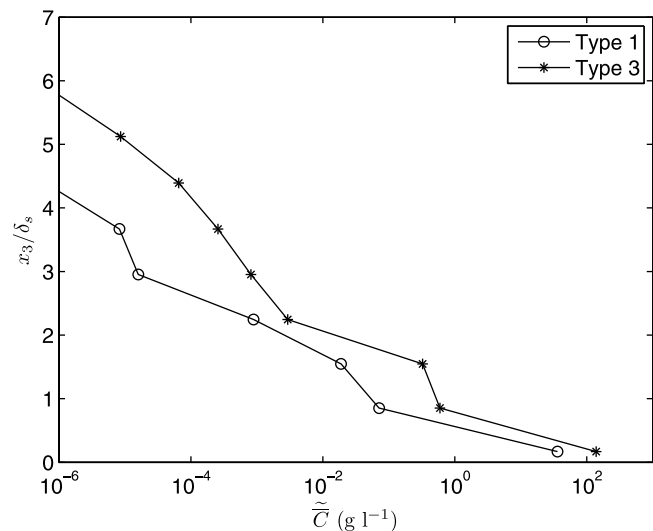
Figure 12. Planform-averaged near-bed sediment concentration profiles in an oscillatory flow at $t = 4.25T$ from simulations with the Type 1 and Type 3 BEMs.

this section we present a resolution study that assesses the importance of the grid resolution on the ability to model bed form evolution. We designate the results of using the Type 1 model as presented in section 4 as the base case, and compare it to the results of using the Type 1 model with four different grid resolutions, namely an isotropic decrease in grid resolution (grid spacing is increased by 4/3 in all three directions), an anisotropic decrease in grid resolution (grid spacing is decreased by a factor of two only in the x_1 and x_3 directions), a reduction in the spanwise grid resolution by a factor of two, and an increase in the resolution in the x_1 and x_3 directions by a factor of two (see Table 2).

[39] Figure 13 depicts the resulting bed forms for all five cases at the end of the sixth wave cycle, which is approximately when the bed forms appear in the base case. The results show that only Case 4 leads to the formation of bed forms that are similar to those in the base case (Figure 13e). This implies that the base case grid resolution is sufficiently resolved because increasing the grid resolution as in Case 4 does not significantly alter the results. For the other cases, although certain nonuniform and somewhat regular patterns are found in Cases 1 and 2, the amplitudes are significantly less than those found in Case 4. In Case 3, a streamwise streak structure is found, which is similar to the bed forms that result with use of the Type 3 BEM and the same resolution as the base case. As the simulations proceed well beyond the time depicted in Figure 13 (not shown), the bed forms in Cases 1, 2, and 3 remain relatively unchanged.

Table 2. Summary of Different Grid Configurations for the Resolution Study in section 6

Case	$N_{x1} \times N_{x2} \times N_{x3}$	Δt (s) ($t = 0 \sim 1T$)	Aspect Ratio ($\Delta x_1 / \Delta x_{3,\min}$)
Base	$320 \times 64 \times 64$	0.001	1.73
1	$240 \times 48 \times 48$	0.002	1.73
2	$160 \times 64 \times 32$	0.002	3.46
3	$320 \times 32 \times 64$	0.001	0.86
4	$480 \times 64 \times 96$	0.001	1.15
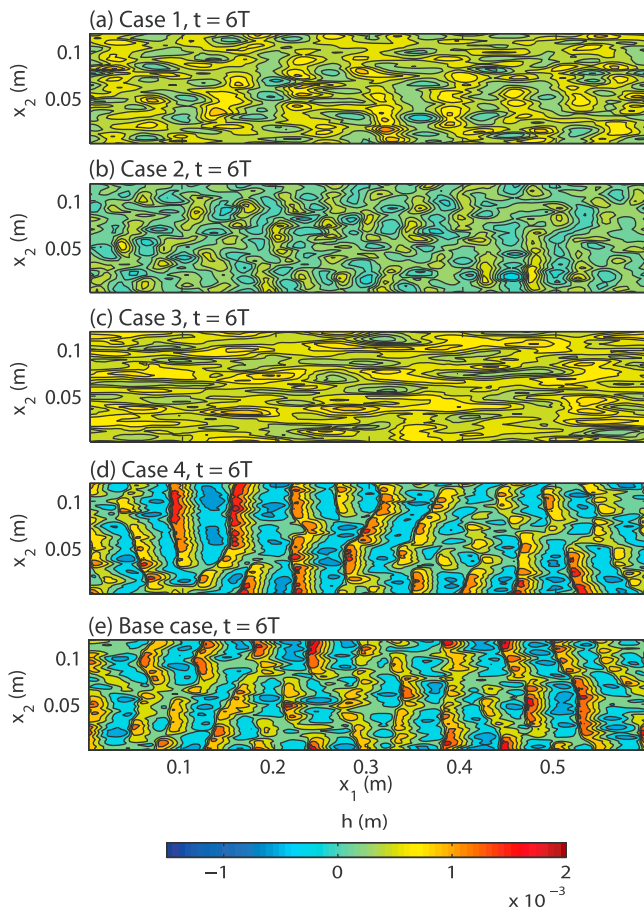
Figure 13. Surface contours of the bed elevation in an oscillatory flow using the Type 1 BEM at $t = 6T$ from (a) Case 1, $N_{x1} \times N_{x2} \times N_{x3} = 240 \times 48 \times 48$; (b) Case 2, $160 \times 64 \times 32$; (c) Case 3, $320 \times 32 \times 64$; and (d) Case 4: $480 \times 64 \times 96$. (e) Base case, $320 \times 64 \times 64$.

[40] Vertical profiles (equation (39)) of suspended sediment concentration with different resolutions averaged over the first wave cycle (indicated by $\langle \rangle$) are plotted in Figure 14. We only show the near-wall region ($x_3/\delta_s < 15$ above the bed) because significant concentrations ($>10^{-6}$ g L^{-1}) after the first wave cycle are confined to a very thin layer near the bed. Other than the upper region in Case 3, no significant differences are found when comparing the near-bed profiles. This demonstrates that although on average suspended sediment transport is similar for each case (other than Case 3), the resulting bed forms vary significantly with grid resolution. This is because a fine grid resolution is essential to resolve the small-scale eddies in the near-wall region for the initiation of bed forms. The profile for Case 3 shows more vertical mixing than others because of the effects of vertical grid resolution on the LES formulation. With coarse vertical resolution, the unresolved subgrid scale turbulence, which is modeled by Smagorinsky-type turbulent diffusion, becomes large and overwhelms the turbulent transport by the resolved flow field.

7. Conclusions

[41] We present a formulation for coupling fluid flow simulation with a sediment transport model that enables the numerical simulation of flow problems with transient bed forms. The method employs large-eddy simulation (LES) for modeling the subgrid scale (SGS) turbulence, the Eulerian approach for modeling the transport of suspended sediment, and a mass balance equation for modeling evolution of the bed elevation. The present approach is implemented in a curvilinear coordinate Navier-Stokes solver in which the bottom boundary can arbitrarily move in response to the complex turbulent flow field above the bed. In order to ensure mass conservation during grid movement, a consistent arbitrary Lagrangian-Eulerian (ALE) scheme with second-order time accuracy is employed to guarantee local conservation of sediment mass. A lid velocity is imposed at the domain top to guarantee global conservation of fluid volume for the incompressible Navier-Stokes solver.

[42] To demonstrate the effectiveness of our approach, bed form evolution is simulated in the presence of oscillatory currents. When fine enough grid resolution is employed, the model reveals several details of the transient process of ripple evolution under waves. Most notably, our model is able to reproduce the transition from two-dimensional to three-dimensional bed forms and the merging of small ripples to form larger ripples. The simulation results agree well with those of laboratory experiments employing similar parameters.

[43] Our approach models the bed elevation through a mass balance equation that ignores the bed load transport formula derived from experiments, and instead relies on the pickup function to account for erosion from the bed. We also include the effects of gravitational settling which effectively amounts to diffusion of bed forms with a diffusion coefficient that depends on the degree to which the bed slope exceeds the angle of repose. Although omission of the bed load transport formula enables realistic simulation of bed forms under an oscillating flow, use of the pickup function to account for near-bed sediment transport relies on sufficient resolution to resolve the near-bed suspended sediment dynamics which effectively acts as a model for bed load transport. Sufficient near-bed resolution of turbulent structures provides the cor-
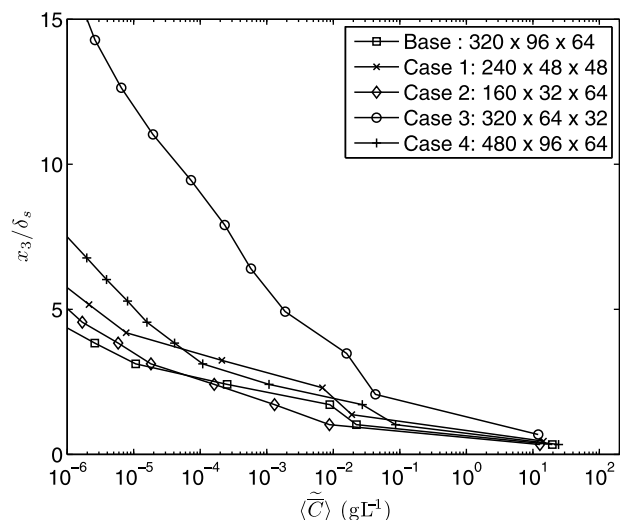
Figure 14. Spatiotemporally averaged near-bed sediment concentration profiles during the first wave cycle from simulations with different grid resolutions.

rect bed shear stress distribution which in turn enables the pickup function to inject the correct amount of suspended sediment into the flow. The high near-bed suspended sediment concentration leads to strong stratification, however, that correctly prevents the near-bed turbulence from becoming too strong and injecting too much sediment into the flow. This behavior is demonstrated via comparison of the Type 1 to the Type 3 bed elevation models (BEMs), the latter of which ignores the effects of stratification. Neglecting stratification effects results in strong spanwise variability and weak streamwise variability as the sediment responds to the turbulent spanwise streaks which are unaffected by stratification, and therefore transport sediment into the water column and inhibit the formation of the important near-bed highly concentrated layer of sediment. If stratification is retained and only bed load transport is included (as in the Type 2 BEM), simulation results of ripple evolution in the presence of oscillatory flow show that the model induces an exceedingly high bed load sediment transport rate, resulting in fast moving ripples with an excessively large initial wavelength. The fast ripple formation results from an overprediction of bed load transport because it is already mostly accounted for by the pickup function and the thin near-bed suspended sediment layer. Inclusion of the bed load model not only overpredicts the growth rate and ripple size, but it prevents the formation of quasi-steady ripples.

[44] While the Type 1 model can predict realistic evolution of bed forms under the action of steady or oscillatory flows, the predictions are only realistic when sufficient grid resolution is employed. As demonstrated by the similarity of the profiles when different grid resolutions are employed, insufficient grid resolution may predict realistic suspended sediment concentration profiles. However, without sufficient grid resolution, near-bed turbulent features are under resolved and the important fine-scale instantaneous shear stress distribution required for bed form initiation is incorrectly computed. Therefore, without sufficient resolution, bed forms do not evolve regardless of the type of BEM that is employed. In addition to an incorrect shear stress distribution, insufficient grid resolution also makes it impossible to resolve the highly concentrated and strongly-stratified near-bed sediment layer that effectively acts as the model for transport of bed load.

Appendix A

[45] Gravity induced sediment flow occurs when the local slope is larger than the angle of repose (θ_{rp}). This flow is zero when the local bed slope is less than θ_{rp}. Therefore, we treat this flow as an avalanche flow down an incline with slope = $\tan\theta_{rp}$. In a two-dimensional configuration, as shown in Figure A1, one can simply model the momentum of the avalanche flow down a slope as

$$\rho_s\left(\frac{\partial u_g}{\partial t} + u_g\frac{\partial u_g}{\partial x}\right) = \rho_s g' \sin\phi_{rp} - \frac{\partial p}{\partial x} + \frac{\partial \tau}{\partial z}, \quad (A1)$$

where the variables associated with the subscript g represent physical quantities for the gravity-induced avalanche flow, δ_B is the thickness of the bed load layer, $g' = g(s-1)/s$ (s is the specific weight of sediment) and all the other variables are as defined in section 2. Assuming that the
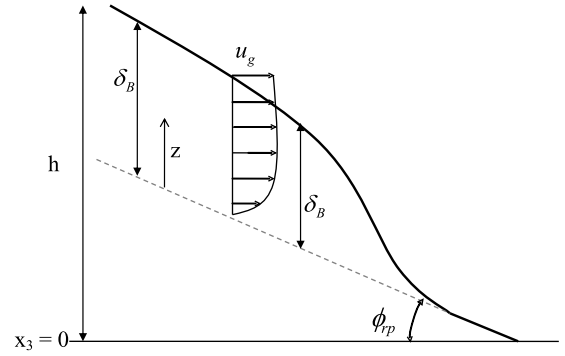
Figure A1. A two-dimensional configuration showing the avalanche flow down an incline to model sediment transport when the local bed slope exceeds the angle of repose, θ_{rp}.

pressure is hydrostatic inside this avalanche flow layer, we have

$$p = \rho_s g' \cos\phi_{rp}(\delta_B - z). \quad (A2)$$

Substitution of equation (A2) into equation (A1) results in

$$\rho_s\left(\frac{\partial u_g}{\partial t} + u_g\frac{\partial u_g}{\partial x}\right) = \rho_s g' \sin\phi_{rp} - \rho_s g' \cos\phi_{rp}\frac{\partial \delta_B}{\partial x} + \frac{\partial \tau}{\partial z}. \quad (A3)$$

Since the nonuniform bed geometry evolves from a flat bed, at the moment when is taken into account, u_g is small, and the avalanche flow time scale is much longer than the flow time scale. Therefore, it is reasonable to ignore the nonlinear and unsteady terms in equation (A3) to obtain the steady state approximation,

$$\frac{\partial \tau}{\partial z} = -\rho_s g' \sin\phi_{rp} + \rho_s g' \cos\phi_{rp}\frac{\partial \delta_B}{\partial x}. \quad (A4)$$

It should be noted that this steady state approximation only applies to the present case in which the local slope is not large enough to induce high-velocity flow. In the case where an abrupt change in geometry is present (e.g., slumping flows), all terms in equation (A3) must be retained. Integrating equation (A4) and using the boundary condition
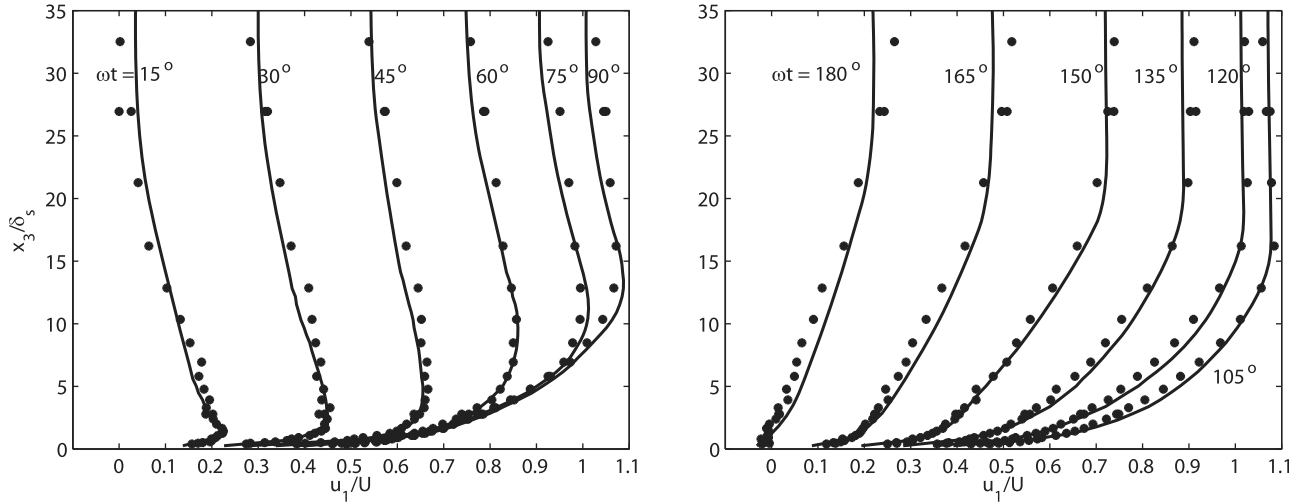
$$\tau|_{z=0} = h\rho_s g' \cos\phi_{rp}\left(\tan\phi_{rp} - \frac{\partial \delta_B}{\partial x}\right), \quad (A5)$$

the shear stress τ is written as

$$\begin{aligned}\tau(z) &= -(z - \delta_B)\rho_s g' \cos\phi_{rp}\left(\tan\phi_{rp} - \frac{\partial \delta_B}{\partial x}\right) \\ &= -(z - \delta_B)\rho_s g' \cos\phi_{rp}\left(-\frac{\partial}{\partial x}(h - \delta_B) - \frac{\partial \delta_B}{\partial x}\right) \quad (A6) \\ &= -(\delta_B - z)\rho_s g' \cos\phi_{rp}\frac{\partial h}{\partial x}.\end{aligned}$$

Assuming Newtonian behavior for the avalanche flow, we have

$$\tau = \mu_s\frac{\partial u_g}{\partial z}, \quad (A7)$$

Figure B1. Planform-averaged streamwise velocity profiles of an oscillatory flow from laboratory observations of *Jensen et al.* [1989] (dots) and the simulation (solid line) using the present model at different time steps in the first wave cycle during flow (left) acceleration and (right) deceleration.

and using the boundary condition $u_b|_{z=0} = 0$, the velocity profile within the avalanche layer is

$$u_g(z) = -\frac{\rho_s g'}{\mu_s}\cos\phi_{rp}\frac{\partial h}{\partial x}\left(\delta_B z - \frac{1}{2}z^2\right), \qquad (A8)$$

where μ_s is the diffusion coefficient for the granular flow. The flow rate Φ_g thus becomes

$$\Phi_g = \int_0^{\delta_B} u_g(z)dz$$
$$= -\frac{\rho_s g'}{3\mu_s}\cos\phi_{rp}\delta_B^3\frac{\partial h}{\partial x}. \qquad (A9)$$

Therefore, when the bed load time scale is large compared to the hydrodynamic time scale and the flow velocity of the gravity-induced granular flow is small, the gravity-induced avalanche flow can be modeled as a diffusion process with the diffusion coefficient $k = \rho_s g'/(3\mu_s)\cos\phi_{rp}\delta_B^3$.

[46] In the above derivation, we have assumed a simple Newtonian flow model to describe the relationship between the shear stress and the velocity gradient (equation (A7)), which may not be true for bed sediment in natural waters. Readers may refer to other references for a comprehensive derivation for non-Newtonian flow models, e.g., the Bingham fluid as a mudflow model [*Liu and Mei*, 1989]. Nevertheless, regardless of the non-Newtonian assumption, it is always possible to derive an equivalent diffusion coefficient to represent gravitational settling as a diffusion process that acts to smooth steep bed forms.

Appendix B

[47] We simulate the turbulent oscillatory boundary layer over a rough wall given by Case 12 of *Jensen et al.* [1989] to validate the present numerical model. Flow is simulated with the same computational setup as in section 4.1 except we apply a different driving pressure gradient to yield an amplitude of the freestream velocity $U_0 = 1.02$ m s^{-1} and a

different oscillatory time period $T = 9.72$ s, which gives a Stokes-layer thickness $\delta_s = \sqrt{2\nu/\omega} = 1.8 \times 10^{-3}$ m. Profiles of the planform-averaged streamwise velocity along with the experimental results are plotted in the first half cycle in Figure B1. Although small differences between model and experimental results are found, in the near-wall region, where the vertical grid size is refined, model results agree well with experimental data. This demonstrates the model capability of obtaining correct planform-averaged flow characteristics by resolving fine-scale features in the near-wall region.

References

Andersen, K. H., M. Abel, J. Krug, C. Ellegaard, L. R. Sondergaard, and J. Udesen (2002), Pattern dynamics of vortex ripples in sand: Nonlinear modeling and experimental validation, *Phys. Rev. Lett.*, *88*(23), 234302.1–234302.4.

Armenio, V., and S. Sarkar (2002), An investigation of stably stratified turbulent channel flow using large-eddy simulation, *J. Fluid Mech.*, *459*, 1–42.

Barr, B. C., D. Slinn, T. Piero, and K. Winters (2004), Numerical simulation of turbulent, oscillatory flow over sand ripples, *J. Geophys. Res.*, *109*, C09009, doi:10.1029/2002JC001709.

Blondeaux, P., and G. Vittori (1991), Vorticity dynamics in an oscillatory flow over a rippled bed, *J. Fluid Mech.*, *226*, 257–289.

Celik, I., and W. Rodi (1988), Modeling suspended sediment transport in nonequilibrium situations, *J. Hydraul. Eng.*, *114*(10), 1157–1191.

Chang, Y. S., and A. Scotti (2003), Entrainment and suspension of sediments into a turbulent flow over ripples, *J. Turbul.*, *4*(19), 1–22.

Chou, Y., and O. B. Fringer (2008), Modeling dilute sediment suspension using large-eddy simulation with a dynamic mixed model, *Phys. Fluids*, 20, 115103.1–115103.13.

Chou, Y., and O. B. Fringer (2010), Consistent discretization for simulations of flows with moving generalized curvilinear coordinates, *Int. J. Numer. Methods Fluids*, 62, 802–826, doi:10.1002/fld.2046.

Chow, F. K., R. L. Street, M. Xue, and J. H. Ferziger (2005), Explicit filtering and reconstruction turbulence modeling for large-eddy simulation of neutral boundary layer flow, *J. Atmos. Sci.*, 62, 2058–2077.

Colombini, R. M. (2004), Revisiting the linear theory of sand dune formation, *J. Fluid Mech.*, 502, 1–16.

Crowe, C. T., T. R. Troutt, and J. N. Chung (1996), Numerical models for two-phase turbulent flows, *Annu. Rev. Fluid Mech.*, 28, 11–43.

Cui, A. (1999), On the parallel computing of turbulent rotating stratified flows, Ph.D. dissertation, Stanford Univ., Stanford, Calif.

Cui, A. Q., and R. L. Street (2001), Large-eddy simulation of turbulent rotating convective flow development, *J. Fluid Mech.*, 447, 53–84.

Cui, A. Q., and R. L. Street (2004), Large-eddy simulation of coastal upwelling flow, *Environ. Fluid Mech.*, 4, 197–223.

Denlinger, R. P., and R. M. Iverson (2004), Granular avalanches across irregular three-dimensional terrain: 1. Theory and computation, *J. Geophys. Res.*, 109, F01014, doi:10.1029/2003JF000085.

Faraci, C., and E. Foti (2002), Geometry, migration and evolution of small-scale bed forms generated by regular and irregular waves, *Coastal Eng.*, 47, 35–52.

Fernandez Luque, R., and R. van Beek (1976), Erosion and transport of bed load sediment, *J. Hydraul. Res.*, 14(2), 127–144.

Fredsoe, J. (1974), On the development of dunes in erodible channels, *J. Fluid Mech.*, 60, 1–16.

Fringer, O. B., and R. L. Street (2005), The dynamics of breaking progressive interfacial waves, *J. Fluid Mech.*, 49, 301–329.

Gessler, D., B. Hall, M. Spasojevic, F. Holly, H. Pourtaheri, and N. Raphelt (1999), Application of a 3-D mobile bed, hydrodynamic model, *J. Hydraul. Eng.*, 125(7), 737–749.

Giri, S., and Y. Shimizu (2006), Numerical computation of sand dune migration with free surface flow, *Water Resour. Res.*, 42, W10422, doi:10.1029/2005WR004588.

Grant, W. D., and O. S. Madsen (1982), Movable bed roughness in unsteady oscillatory flow, *J. Geophys. Res.*, 81(C1), 469–481, doi:10.1029/JC087iC01p00469.

Hodges, B. R., and R. L. Street (1999), On simulation of turbulent nonlinear free-surface flows, *J. Comput. Phys.*, 151, 425–457.

Jensen, B. L., B. M. Sumer, and J. Fredsoe (1989), Turbulent oscillatory boundary layers at high Reynolds numbers, *J. Fluid Mech.*, 206, 265–297.

Kim, J., and P. Moin (1985), Application of a fractional-step method to incompressible Navier-Stokes equations, *J. Comput. Phys.*, 59, 308–323.

Lacy, J. R., D. M. Rubin, H. Ikeda, K. Modukai, and D. Hanes (2007), Bed forms created by simulated waves and currents in a large flume, *J. Geophys. Res.*, 112, C10018, doi:10.1029/2006JC003942.

Leonard, B. P. (1979), A stable and accurate convective modeling procedure based on quadratic upstream interpolation, *Comput. Meth. Appl. Mech. Eng.*, 75, 369–392.

Leonard, B. P. (1988), Simple high-accuracy resolution program for convective modelling of discontinuities, *Int. J. Numer. Methods Fluids*, 8, 1291–1318.

Liu, K. F., and C. C. Mei (1989), Slow spreading of a sheet of Bingham fluid on an inclined plane, *J. Fluid Mech.*, 207, 505–529.

Mangeney-Castelnau, A., F. Bouchut, J. P. Vilotte, E. Lajeunesse, A. Aubertin, and M. Pirulli (2005), On the use of Saint Venant equations to simulate the spreading of a granular mass, *J. Geophys. Res.*, 110, B09103, doi:10.1029/2004JB003161.

Meyer-Peter, E., and R. Mueller (1948), Formulas for bed load transport, in *Proceedings of the 2nd Meeting of the International Association for Hydraulic Research*, Stockholm, 7–9 Jul.

Nakayama, A., K. Hori, and R. L. Street (2004), Filtering and LES of flow over irregular rough boundary, paper presented at Summer Program at Center for Turbulence Research, NASA Ames, Stanford Univ., Stanford, Calif.

O'Donoghue, T., and G. S. Clubb (2001), Sand ripples generated by regular oscillatory flow, *Coastal Eng.*, 44, 101–115.

Ortiz, P., and P. K. Smolarkiewicz (2006), Numerical simulation of sand dune evolution in severe winds, *Int. J. Numer. Methods Fluids*, 50, 1229–1246.

Perng, C. Y., and R. L. Street (1989), 3-D unsteady flow simulation: Alternative strategies for a volume-average calculation, *Int. J. Numer. Methods Fluids*, 9, 341–362.

Pitman, E. B., C. C. Nichita, A. Patra, A. Bauer, M. Sheridan, and M. Bursik (2003), Computing granular avalanches and landslides, *Phys. Fluids*, 12, 3638–3642.

Ribberink, J. S. (1998), Bed-load transport for steady flows and unsteady oscillatory flows, *Coastal Eng.*, 34, 59–82.

Ridchards, K. J. (1980), The formation of ripples and dunes on an erodible bed, *J. Fluid Mech.*, 99, 597–618.

Scandura, P. G., G. Vittori, and P. Blondeaux (2000), Three-dimensional oscillatory flow over steep ripples, *J. Fluid Mech.*, 412, 335–378.

Smith, J. D., and S. R. McLean (1977), Spatially averaged flow over a wacy surface, *J. Geophys. Res.*, 82(12), 1735–1746, doi:10.1029/JC082i012p01735.

Soulsby, R. (1997), *Dynamics of Marine Sands: A Manual for Practical Applications*, Telford, London.

Testik, F. Y., S. I. Voroparev, and H. J. Fernando (2005), Adjustment of sand ripples under changing water waves, *Phys. Fluids*, 17, 072104.1–072104.8.

van Rijn, L. C. (1993), *Principles of Sediment Transport in Rivers, Estuaries, and Coastal Seas*, Aqua, Amsterdam.

Whitehouse, R. J. S., and J. Hardisty (1988), Experimental assessment of two theories for the effect of bedslope on the threshold of bed load transport, *Mar. Geol.*, 79, 135–139.

Wilson, K. C. (1987), Analysis of bed load motion at high shear stress, *J. Hydraul. Div.*, 113(1), 97–103.

Wu, W., W. Rodi, and T. Wenka (2000), 3-D numerical modeling of flow and sediment transport in open channels, *J. Hydraul. Eng.*, 126(1), 4–15.

Zang, Y., and R. L. Street (1995), Numerical simulation of coastal upwelling and interfacial instability of a rotating and stratified fluid, *J. Fluid Mech.*, 305, 47–75.

Zang, Y., R. L. Street, and J. R. Koseff (1993), A dynamic mixed subgrd-scale model and its application to turbulent recirculation flows, *Phys. Fluids*, 5, 3186–3196.

Zang, Y., R. L. Street, and J. R. Koseff (1994), A nonstaggered grid, fractional step method for time-dependent incompressible Navier-Stokes equations in curvilinear coordinates, *J. Comput. Phys.*, 18–33.

Zedler, E. A., and R. L. Street (2001), Large-eddy simulation of sediment transport: Currents over ripples, *J. Hydraul. Eng.*, 127(6), 444–452.

Zedler, E. A., and R. L. Street (2006), Sediment transport over ripples in oscillatory flow, *J. Hydraul. Eng.*, 132(2), 1–14.

Y.-J. Chou and O. B. Fringer, Environmental Fluid Mechanics Laboratory, Stanford University, Stanford, CA 94305-4020, USA. (yjchou@stanford.edu)